A third of organic carbon is mineral-bound in permafrost sediments exposed by the world's largest thaw slump, Batagay, Siberia

Maxime Thomas[1*], Loeka L. Jongejans[2,3], Jens Strauss[2], Chloé Vermylen[1], Sacha Calcus[1], Thomas Opel[4], Alexander Kizyakov[5], Sebastian Wetterich[2,6], Guido Grosse[2,3], Sophie Opfergelt[1]

[1] Earth and Life Institute, Université catholique de Louvain, Louvain-la-Neuve, Belgium
[2] Permafrost Research Section, Alfred Wegener Institute Helmholtz Centre for Polar and Marine Research, Potsdam, Germany
[3] Institute of Geosciences, University of Potsdam, Potsdam, Germany
[4] Polar Terrestrial Environments Section, Alfred Wegener Institute Helmholtz Centre for Polar and Marine Research, Potsdam, Germany
[5] Lomonosov Moscow State University, Cryolithology and Glaciology Department, Faculty of Geography, Moscow, Russia
[6] Current address: Technische Universität Dresden, Institute of Geography, Dresden, Germany

*Corresponding author: Maxime Thomas: maxime.thomas@uclouvain.be | ORCID: 0000-0002-3661-8203
Croix du Sud, 1 bte L7.05.10, B-1348 Louvain-la-Neuve, Belgium | Phone: +32 (0)10 47 36 29

Loeka L. Jongejans | loeka.jongejans@live.nl | 0000-0002-0383-4567
Jens Strauss | jens.strauss@awi.de | 0000-0003-4678-4982
Chloé Vermylen | chloe.vermylen7@gmail.com
Sacha Calcus | sacha.calcus@student.uclouvain.be
Thomas Opel | thomas.opel@awi.de | 0000-0003-1315-8256
Alexander Kizyakov | akizyakov@mail.ru | 0000-0003-4912-1850
Sebastian Wetterich | sebastian.wetterich@mailbox.tu-dresden.de | 0000-0001-9234-1192
Guido Grosse | guido.grosse@awi.de | 0000-0001-5895-2141
Sophie Opfergelt | sophie.opfergelt@uclouvain.be | 0000-0002-1773-4823

Abstract

Organic carbon (OC) in permafrost interacts with the mineral fraction of soil and sediments, representing < 1% to ~80% of the total OC pool. Quantifying the nature and controls of mineral-OC interactions is therefore crucial for realistic assessments of permafrost-carbon-climate feedbacks, especially in ice-rich regions facing rapid thaw and the development of thermo-erosion landforms. Here, we analyzed sediment samples from the Batagay megaslump in East Siberia and we present total element concentrations, mineralogy, and mineral-OC interactions in its different stratigraphic units. Our findings indicate that up to 34 ± 8% of the OC pool interacts with mineral surfaces or elements. Interglacial deposits exhibit enhanced OC-mineral interactions, where OC has undergone greater microbial transformation and has likely low degradability. We provide a first order estimate of ~ 12 000 tons of OC mobilized annually downslope of the headwall (i.e., the approximate mass of 30 large aircrafts), with a maximum of 38% interacting with OC via complexation with metals or associations to poorly crystalline iron oxides. These data imply that over one-third of the OC exposed by the slump isn't readily available for mineralization, potentially leading to prolonged OC residence time in soil and sediments under stable physicochemical conditions.

Keywords: thermo-erosion, mineral-organic carbon interactions, Batagay, retrogressive thaw slumps, iron, headwall

1. Introduction

Recent studies have shown that, due to the Arctic amplification, air temperature increase is occurring nearly four times faster in the Arctic than the global average increase since 1979 (Rantanen et al., 2022). Ice-rich permafrost is particularly sensitive to warming and subsequent rapid thaw process (e.g., Dobricic and Pozzoli, 2019; IPCC, 2019; Turetsky et al., 2019) and contains thousands of years old organic carbon (OC) which can be mobilized by various thaw processes (e.g., Abbott and Jones, 2015; Koven et al., 2011; Lawrence et al., 2015; McGuire et al., 2018; Schuur et al., 2015; Turetsky et al., 2020; Vonk et al., 2013a, 2012). This OC pool in the northern permafrost-affected regions is estimated to range from 1460 to 1600 Pg carbon (i.e., roughly half of the global soil carbon pool and twice as much as the carbon currently stored in the atmospheric pool; Hugelius et al., 2014; Strauss et al., 2021a). Existing estimates indicate that 5-15% of the terrestrial OC reservoir would be vulnerable to being emitted as greenhouse gases by the end of this century (Plaza et al., 2019; Schuur et al., 2015), inducing a positive permafrost-carbon-climate feedback. These assessments are based on simulated volumes of OC that will be exposed by the increase in thickness of the seasonally thawing active layer, by a process commonly referred to as gradual thawing. Rapid thaw processes such as thermokarst , thermo-denudation and thermo-erosion may account for additional release of OC and greenhouse gases not yet accounted for in models simulating gradual thaw (Turetsky et al., 2020, 2019). Various factors determine how much of the thawed OC eventually is transformed into greenhouse gases, such as microbial activity (e.g., Patzner et al., 2022), soil hydrology and redox state (e.g., Schädel et al., 2016; Vonk et al., 2019), and OC sources and quality (e.g., Bröder et al., 2022; Jongejans et al., 2022a). The future trajectory of permafrost carbon emissions yet also depends on the proportion of the free OC pool relative to the proportion of mineral-interacting forms of OC (Opfergelt, 2020), as well as the potential contribution of previously perennially frozen deep carbon as a consequence of ice-rich permafrost thaw (Natali et al., 2021).

By contrast to gradual thaw that occurs across the Arctic, physical degradation of ice-rich permafrost are more punctual events in both time and space, which is why they are sometimes referred to as abrupt thaw events. Such physical degradations – named thermokarst landforms (Heginbottom et al., 2012; Kokelj and Jorgenson, 2013) – are the consequence of ground collapse and subsidence caused by the loss of the cementing properties of the melting excess ice in the ground. One of these types of physical degradations are retrogressive thaw slumps (RTS), which are amongst the most dynamic forms of thermo-erosion and thermo-denudation, sometimes also referred to as hillslope thermokarst (Kokelj et al., 2016; Kokelj and Jorgenson, 2013). Recent research indicates that under the SSP58.5 scenario (the Shared

Socio-economic Pathway (SSP) corresponding to very high greenhouse gas emissions scenario; Fox-Kemper et al., 2021), the area susceptible to be affected by hillslope thermokarst landforms is projected to increase by ~ 250,000 km² by the end of the 21st century, but despite the rather small total area it may account for one third of all thermokarst-related carbon losses (Turetsky et al., 2020). These phenomena are important to consider in the permafrost carbon budget since this exposed deep OC pool is tens of thousands of years old and would not have re-entered the modern carbon cycle if these disturbances had not occurred, i.e. under gradual permafrost thaw. They could significantly increase carbon emissions from thawing permafrost and compromise the feasibility of remaining below 1.5°C or 2°C targeted by the Paris Agreement (Natali et al., 2021).

Retrogressive thaw slumps are landforms that enlarge due to thawing of frozen deposits and melting of ground ice at a headwall, producing slumping and sediment flow through meltwater streams and mudflows, potentially accumulating in a scar zone or form a mudlobe at the toe of the RTS. Thaw slumping can be initiated, e.g., by either lateral or thermal erosion by water (Kokelj and Jorgenson, 2013); active layer detachment following heavy precipitation (Lacelle et al., 2010); and human activity such as road construction, mining, or deforestation (Burn and Lewkowicz, 1990). The retreat of the collapse front each summer can reach several (tens of) meters per year (Brooker et al., 2014; Günther et al., 2015; Kokelj et al., 2021; Kunitsky et al., 2013; Lacelle et al., 2015; Leibman et al., 2021; Vadakkedath et al., 2020; van der Sluijs et al., 2023, 2018). These structures therefore expose and relocate large volumes of material (Kokelj et al., 2021, 2015a; Shakil et al., 2020; Tanski et al., 2017; van der Sluijs et al., 2018), such as thawed sediments or melt water, and involve masses of previously perennially frozen carbon in the form of plant and animal remains, until they stabilize. In recent years, increased precipitation in certain Arctic areas has accentuated the development of mega-slumps and downslope sediment transport in debris tongues (Kokelj et al., 2021, 2015b). These debris tongues can be maintained stable for decades or even centuries (Murton and Ballantyne, 2017) and contain OC that is partially bound to minerals (e.g., Mu et al., 2020, 2016; Shakil et al., 2022; Thomas et al., 2023) via OC-mineral interactions.

Soil OC can be conceptualized into a free particulate pool, and a pool of mineral-interacting forms of OC (Lavallee et al., 2020). The latter represents a potentially stabilized OC pool with reduced susceptibility to microbial degradation (e.g., García-Palacios et al., 2024; Keil and Mayer, 2014; Kleber et al., 2015; Lalonde et al., 2012; Lavallee et al., 2020; Schmidt et al., 2011) which is less likely to contribute to the permafrost-carbon-climate feedback. A recent study has shown that OC in cold regions appears to be distributed mainly in the more vulnerable particulate pool, rather than in the more persistent mineral-interacting pool of OC (García-Palacios et al., 2024).Those mineral-interacting forms of OC, however, remain highly variable at the Arctic scale (i.e., accounting for ~1 % to ~ >80 % of permafrost soils and sediments total OC; Dutta et al., 2006; Mueller et al., 2015; Salvadó et al., 2015), and can be divided into three categories: (i) organo-metallic complexes resulting from the complexation of OC with metal ions (i.e., OC complexed with e.g. Al, Fe, Mn; Courchesne and Turmel, 2008; Lützow et al., 2006); (ii) organo-mineral associations (Kleber et al., 2015) resulting from the interaction of OC with mineral surfaces (such as OC sorbed onto clay minerals or Fe-oxides, using cation bridges such as Ca or Mg) and (iii) OC physical protection within soil aggregates which renders OC spatially inaccessible for microorganisms (i.e., occluded, involving clay minerals, Fe-Al (hydr)oxides or carbonates in aggregates; von Lützow et al., 2006). The free particulate and mineral-interacting forms of organic matter pools are highly contrasted concerning for example their physical and chemical properties, mean residence times in soil, and responses to land use change. It is estimated that particulate organic matter has a mean residence time ranging from a few years to decades, while it persists for decades to centuries for mineral-interacting forms of OC (e.g., Kleber et al., 2015; Kögel-Knabner et al., 2008; Lavallee et al., 2020). It is worth pointing out that the capability of organic matter to be decomposed also depends on its molecular recalcitrance (i.e., some compounds are inherently stable, e.g., aromatic compounds) but this is thought not to be the dominant mechanism of OC stabilization (e.g., Keil and Mayer, 2014; von Lützow et al., 2006).

Within a thaw slump headwall, the exposed sediments are often stratified into different layers that correspond to different depositional regimes and ages. The environmental conditions at the time of deposition, past permafrost dynamics since deposition and the chemical composition of the sediment will control the nature and amount of OC interacting with the soil/sediments mineral pool. Studying at high vertical resolution the proportion and nature of OC-mineral interactions within such deposits of different ages and lithologic nature is therefore a key step in establishing an enhanced understanding of the carbon balance of material mobilized from such rapid erosion landforms and determining which proportion of the mobilized OC is interacting with the mineral pool as well as the mechanisms involved.

Here, we determine the mechanism for OC-mineral interactions within the sediments of the world's largest known retrogressive thaw slump (Kunitsky et al., 2013), the Batagay megaslump in East Siberia, exposing the second oldest directly dated permafrost in the Northern Hemisphere (from ~650 ka to the modern day; Murton et al., 2022).

2. Methods

2.1. Study area and site description

The Batagay thaw slump, situated about 10 km southeast of Batagay settlement in Yakutia (**Figure 1** a-b), is located on a northeast-facing hillslope. Based on retrospective remote sensing data analysis; the RTS was formed in the end of 1990-s as a bowl-shaped landform (Kunitsky et al., 2013; Savvinov et al., 2018) at the place of previously existing thermo-erosional gully. The gully and subsequently the slump formed over around 40 years. In 2019, it exposed an about 55 m high headwall (Kizyakov et al., 2023; Murton et al., 2023). Following the Köppen (1884) climate classification, the area of Batagay is characterized by a subarctic continental climate which implies relatively low precipitation and a particularly wide seasonal temperature gradient. For a period ranging from 1988 to 2017, the site had a mean winter temperature of -40.0°C (December to February), a mean summer temperature of 13.7°C (July to August) and a mean annual temperature of -12.4°C. For the same period, the mean annual precipitation was 203 mm, and the mean summer precipitation 106 mm (Murton et al., 2023).

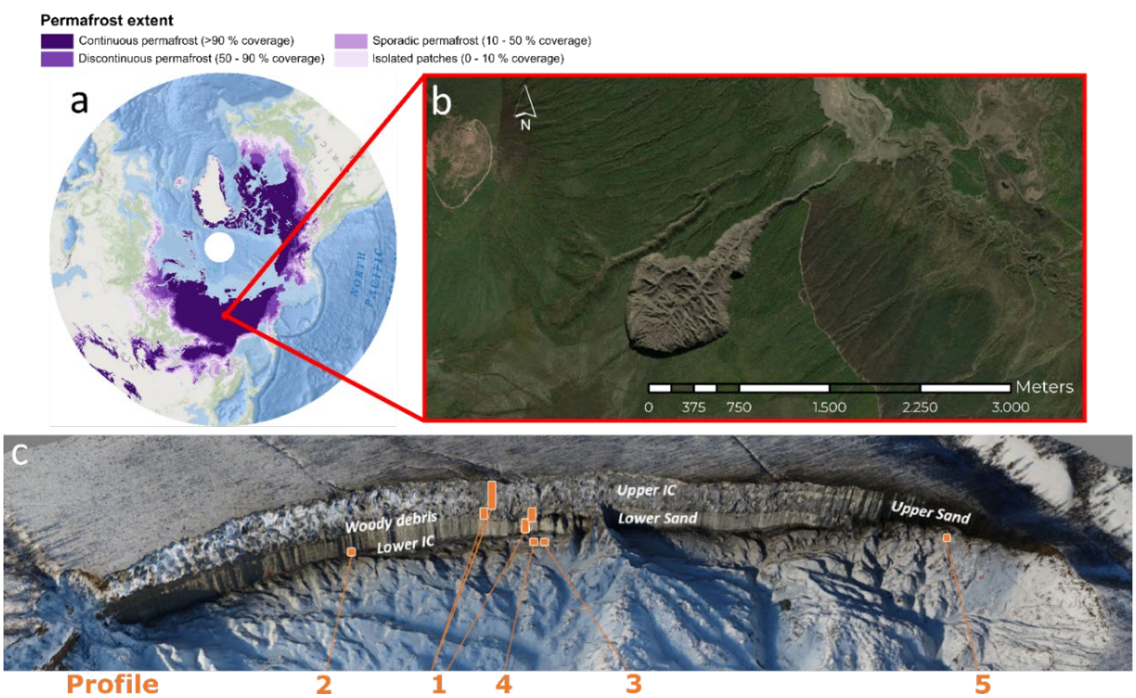

Figure 1 | *Batagay thaw slump location, extent, morphology and sampling locations. **a**) Permafrost extent in the Northern Hemisphere (Obu et al., 2018) and **b**) thaw slump extent and morphology. Map created in ArcMap 10.8. Basemap layer credits: World Ocean Base in **a**): Esri, GEBCO, NOAA, National Geographic and other contributors. World Imagery in **b**): ESRI satellite image basemap; **c**) Overview of sediments samples at the west wall of the Batagay slump, photo: A. Kizyakov, 24.03.2019. Sediment samples were collected from a main profile (profile 1). An additional series of sediment samples was taken from the slump bottom (profile 2), i.e., vertically below the main profile. Additional discrete sediment samples were taken in profiles from blocks in the slump bottom (profiles 3, 4) and a baydzherakh, i.e., a frozen thermokarst mound (Profile 5) (panel c modified from Jongejans et al., 2021).*

The headwall provides access to frozen stratigraphically discontinuous deposits from the Middle Pleistocene (~650 ky) to the Holocene (Murton et al., 2022) and consists of six distinct stratigraphic units (Murton et al., 2023, 2022). Those stratigraphic units have been extensively described in Murton et al. (2023). Briefly, at the slump bottom, the Lower Ice Complex (LIC; ∼3–7m thick) is only exposed at the deepest part of the main headwall and probably still buried for the main part. The LIC developed during the early Middle Pleistocene (MIS 16) or earlier and has survived multiple interglacials, including the super-interglacial MIS 11c. Above the LIC lies the Lower Sand Unit (LSU; ~ 20 m thick) with horizontally layered sand and thinner ice and composite wedges compared to those of the LIC. The LSU is covered by the Woody Debris layer (WD; MIS 5e), which is laterally discontinuous and present in a few lenses up to 3 m thick, consisting of wood remains with branches and twigs. It is overlain by the Upper Ice Complex (UIC; ∼20–25 m thick, MIS 4-2). This is the local equivalent of the late Pleistocene Yedoma ice complex, widespread in Siberia and Alaska, and is dominated by large syngenetic ice wedges embedded within silty and sandy sediments (Strauss et al., 2021b). Total volumetric ice content of the UIC is up to about 87%, of which up to 70,2% is wedge-ice volume (Kizyakov et al., 2023). Above the UIC, and only exposed downslope of the main headwall in the northern and southern parts of thaw slump, there is the Upper Sand Unit (USU) of MIS 3 to 2 origin, which was not sampled for this study. Finally, the brown and sandy Holocene Cover (HC) composed of sandy sediments covers the UIC, including a 0.2 to ~1.4 m thick active layer. The top layer (5 cm) is referred to as the organic layer (OL). In the following, we distinguish (after Jongejans et al., 2022) between interglacial units comprising the organic layer, the Holocene Cover and Woody Debris layer and units deposited during glacial periods, which are the Upper and Lower Ice Complexes, and the Lower Sand Unit.

2.2. Sampling locations

Samples were collected during field work from March 18 to April 4, 2019 (Jongejans et al., 2021) along a vertical profile with sample spacing every half a meter for the upper 10 m of the headwall and then every meter due to greater homogeneity beyond 10 m in terms of sedimentology and cryostratigraphy (profile P1, n = 53; **Figure 1**c; **Table 1**). Sampling was carried out via abseiling from a rope attached to the top of the headwall, using a hole saw (ø57 mm, 40 mm depth) mounted on a Makita power drill. At each sampled depth, three cores were taken next to each other and have already been analyzed for biomarkers and sedimentology in Jongejans et al. (2022a). The depths have been calibrated taking into account angles of the wall and rearrangement of the tape-measure and are given in cm below surface. An additional series of samples (profile 2, n = 7; **Figure 1**c; **Table 1**) was taken from the slump bottom, i.e., vertically below the profile P1. These correspond to samples from the LIC (below the thaw unconformity (see section **2.1**) and the LSU. Additional discrete sediment samples were taken in profiles from huge frozen blocks in the slump bottom (Profile 3, n = 4; Profile 4, n = 3; **Figure 1**c; **Table 1**) which could be stratigraphically attributed to their original position in the headwall and a baidzherakh, i.e., a frozen thermo-erosional mound (Profile 5, n = 3; **Figure 1**c; **Table 1**) (Jongejans et al., 2021, 2022a).

Table 1 | *Overview of the number of samples collected, associated depth, stratigraphic unit origin and age (MIS= Marine isotope stages; n = number of samples)*

Profile	Stratigraphic units	Age*		Depth (cm)	n	Total n
		MIS	ka			
1	Organic layer		modern	5	1	53
	Holocene Cover	MIS 1	0.39	15 – 195	6	
	Upper Ice Complex (Yedoma)	MIS 4-2	at least 60 to 30	260 – 2882	31	
	Woody Debris layer	MIS 5e (last interglaciation)	~125	3012 – 3259	5	
	Lower Sand Unit	MIS 16-6	~175	3350 – 4942	10	
2	Lower Sand Unit	MIS 16-6	~175	5100 – 5150	2	7
	Lower Ice Complex	MIS 16 or earlier	at least 650	5170 – 5310	5	
3	Upper Ice Complex (Yedoma)				2	4
	Woody Debris layer				2	
4	Woody Debris layer				1	3
	Lower Sand Unit				2	
5	Upper Ice Complex (Yedoma)				3	3
					total	70

* based on Murton et al. (2022)

2.3. Mineralogy and bulk element concentrations

The X-ray diffraction (XRD) method allows the characterization of the presence of crystalline mineral phases. This technique is used to determine the atomic and molecular structure of a crystal by analyzing the diffraction pattern produced when X-rays interact with a crystalline material. The diffraction pattern enables the identification of minerals and their relative abundances in the sample. We assessed the mineralogy on finely ground bulk sediments from at least one sample out of two along the profile 1 (n = 34), and all samples in profiles 2, 3, 4 and 5 (n = 17). The mineralogy of the bulk samples was determined on non-oriented powder finely ground in a mortar (Cu Kα, Bruker Advance D8 diffractometer, detection limit 5 % by weight).

We measured the total concentrations of Ca, Fe, Al and Mn in all samples (n = 70) using a portable X-ray fluorescence (XRF) device (*Niton XL3t GOLDD* + pXRF; ThermoFisher Scientific, Waltham, the United States). The measurements were performed in laboratory (ex-situ) conditions on air-dried samples to avoid introduction of additional variability (e.g., water content, sample heterogeneity). Briefly, samples were placed on a circular plastic cap (2.5 cm diameter), its base covered with a thin transparent film (prolene 4 µm). Minimum sample thickness in the cap was set to 2 cm to prevent underestimation of the detected intensities (Ravansari et al., 2020) and total time of analysis is set to 90 s to standardize each measurement.

The pXRF-measured concentrations were calibrated using a method following Monhonval et al. (2021a). A linear regression was used to correct pXRF concentrations for trueness on all samples (n = 70). This regression was obtained based on element concentrations measured by pXRF and by inductively coupled plasma optical-emission spectrometry (ICP-OES) after alkaline fusion on samples from different permafrost environments, including 13 samples from this study (robust $R^2 \geq 0.9$ for Fe, Ca, ; robust $R^2 \geq 0.8$ for Mn; robust $R^2 \geq 0.6$ for Al ; Figure S. 1). In the following, the total element concentration measured by XRF and corrected for trueness will be referred to as Ca_t, Mn_t, Al_t, Fe_t. A complete description of the sites used, and the calibrations can be found in the supplementary information S1.

The total organic carbon (TOC) content on sediments was determined after homogenization of freeze-dried samples using aVario TOC Cube Elemental Analyser and expressed in wt%, like reported in Jongejans et al. (2022b). We acknowledge that the analyses presented in this study focus solely on the soil/sediment fraction of the permafrost samples and not on the organic carbon present, for example, in ice-wedges. In the following, the TOC presented is the TOC present in sediments only.

2.4. Selective extractions

Two procedures of selective extraction from soil were used as indicators of the complexed and poorly crystalline oxides phases (Rennert, 2019). More specifically: (i) the sodium pyrophosphate extraction of Fe, Al and Mn targets the organo-metallic complexes (Bascomb, 1968; Parfitt and Childs, 1988). We acknowledge a possible contribution of oxide nanoparticles in addition to the organically-bound metals (Courchesne and Turmel, 2008; Jeanroy and Guillet, 1981; Kaiser and Zech, 1996), but limited by centrifugation and filtration of the extract; (ii) the dark ammonium oxalate extraction of Fe targets poorly crystalline oxides (i.e., poorly crystalline oxides and organo-metallic complexes; Blakemore et al., 1981). The pool of mineral elements that form organo-metallic complexes or associations with OC are often referred to as "reactive". This reactive pool combines all poorly crystalline, amorphous, and complexed forms of Fe, Mn, and Al and corresponds here to the ammonium oxalate extraction.

Those two selective extractions were carried out on at least one sample out of two in the profile 1 (n = 37; **Figure S. 2**) and all samples in profiles 2, 3, 4 and 5 (n = 17). Concentrations in Fe, Al and Mn were measured in solution by ICP-OES after each selective extraction. In the following, the elements extracted by pyrophosphate and oxalate methods will be referred to as the corresponding element symbol followed by a subscripted letter indicating the type of extraction, namely 'p' for pyrophosphate extraction (Fe_p, Al_p, Mn_p) and 'o' for oxalate extraction (Fe_o).

The pool of OC selectively extracted with sodium pyrophosphate (Bascomb, 1968; Jeanroy and Guillet, 1981; Parfitt and Childs, 1988) and dark ammonium oxalate (Blakemore et al., 1981) was measured on the same solutions as those used for the selective extractions of metals (n = 54; section **2.5**). Briefly, (i) for carbon involved in organo-metallic complexes, we measured dissolved OC released after dispersion by pyrophosphate using a Shimadzu TOC-L analyzer (measuring non-purgeable OC). In the following, this carbon extracted by pyrophosphate will be referred to as C_p; (ii) for oxalate extracted carbon, we measured the absorbance at 430 nm in the oxalate extract (via a Genesys 10 S VIS spectrophotometer, with the extractant solution as a blank) to evaluate the organic acid concentration. The optical density of the oxalate extract (ODOE) is mainly influenced by the extracted fulvic acids thereby indicating the concentration in organic acids present in the oxalate extract (Daly, 1982).

2.5. First order estimate of the material eroded by the retreat of the headwall

Using the sampling depths along the headwall and an estimate of the retreat rate of the collapse front (Vadakkedath et al., 2020), we established a first order estimate of the annual mass balance assessment of the material eroded from the slump. We first partitioned the wall into horizontal slices using the thickness (m) between different sampling depths, which we multiplied by an average expansion rate of the slump (0.026 km²/yr on average between 1991 and 2018;

Vadakkedath et al., 2020) to obtain an annual volume of sediment mobilized from each slice. From each slice, we then removed an average volume proportion of ice wedges per stratigraphic unit, following Kizyakov et al. (2023), i.e., 67% for the Upper Ice Complex, 9% for the Lower Sand Unit and 56% for the Lower Ice Complex. We then estimated the mass of sediment mobilized annually by each slice by multiplying the annual volume mobilized by the bulk density (Eq. 1). The bulk density was determined by using an inverse relationship with porosity, assuming that pore volume in ice-saturated (i.e., >20% volume) samples is directly measured with pore ice volume (see full method in Strauss et al., 2013). If ice content was not measured on the sample, the mean value of the stratigraphic unit was assigned.

Equation 1 |

$$\begin{aligned} &\mathit{sediment\ mass\ retreat\ rate\ slice}_i \left(\frac{kg_{sediment}}{yr}\right) \\ &= \mathit{thickness\ slice}_i\ (m) \times \left(1 - \mathit{ice\ wedge\ volume\ proportion\ slice}_i \left(\frac{m^3}{m^3}\right)\right) \times \mathit{average\ expansion\ rate} \left(\frac{m^2}{yr}\right) \\ &\times \mathit{bulk\ density\ slice}_i \left(\frac{kg}{m^3}\right) \end{aligned}$$

To establish the budget for the mobilization of OC and mineral elements as total, complexed, poorly crystalline oxides phases, we multiplied the concentration of each element $\left(\frac{kg_{element}}{kg_{sediment}}\right)$ by the result of Eq. 1 $\left(\frac{kg_{sediment}}{yr}\right)$. If the selective extraction was not performed on the sample, the mean value of the stratigraphic unit was assigned. We then summed the contributions from each slice to obtain an estimate of the total mass mobilized each year by the slump for the different elements as total, complexed, poorly crystalline oxides phases (Eq. 2).

Equation 2 |

$$\mathit{total\ element\ mass\ retreat\ rate} \left(\frac{kg_{element}}{yr}\right) = \sum_{i\ slices} \mathit{element\ concentration\ slice}_i \left(\frac{kg_{element}}{kg_{sediment}}\right) \times \mathit{slice}_i\ \mathit{sediment\ mass\ retreat\ rate} \left(\frac{kg_{sediment}}{yr}\right)$$

2.6. Statistical Analysis

We performed computations for statistical analysis using R software version R.3.6.1 (R Core Team, 2019). Compact displays of data distributions were performed using boxplots showing five summary statistics: the median, two hinges for the 25th and 75th percentiles and two whiskers that extend from the hinges to 1.5 times the inter-quartile range (Hintze and Nelson, 1998; McGill et al., 1978). Robust linear regression (R^2 adj) presented in this study are implemented with an alpha of 0.95. When numerical statistics are presented in the text for dataset descriptions, the mean ± standard deviation of the distribution is presented. For comparing two datasets, we performed nonparametric statistical Wilcoxon test.

3. Results

3.1. Mineralogy and bulk element concentrations

In all stratigraphic units, the diffractograms indicate the presence of primary silicate minerals (quartz, pyroxene, sodium-, calcium- and potassium- feldspars and micas), secondary silicate minerals (kaolinite, illite, vermiculite), sulfates (anhydrite) and, often, carbonates (dolomite). Those mineral species are detected in profile 1 (**Figure 2**), profile 2 (**Figure S. 3**) and profiles 3-4-5 (**Figure S. 4**).

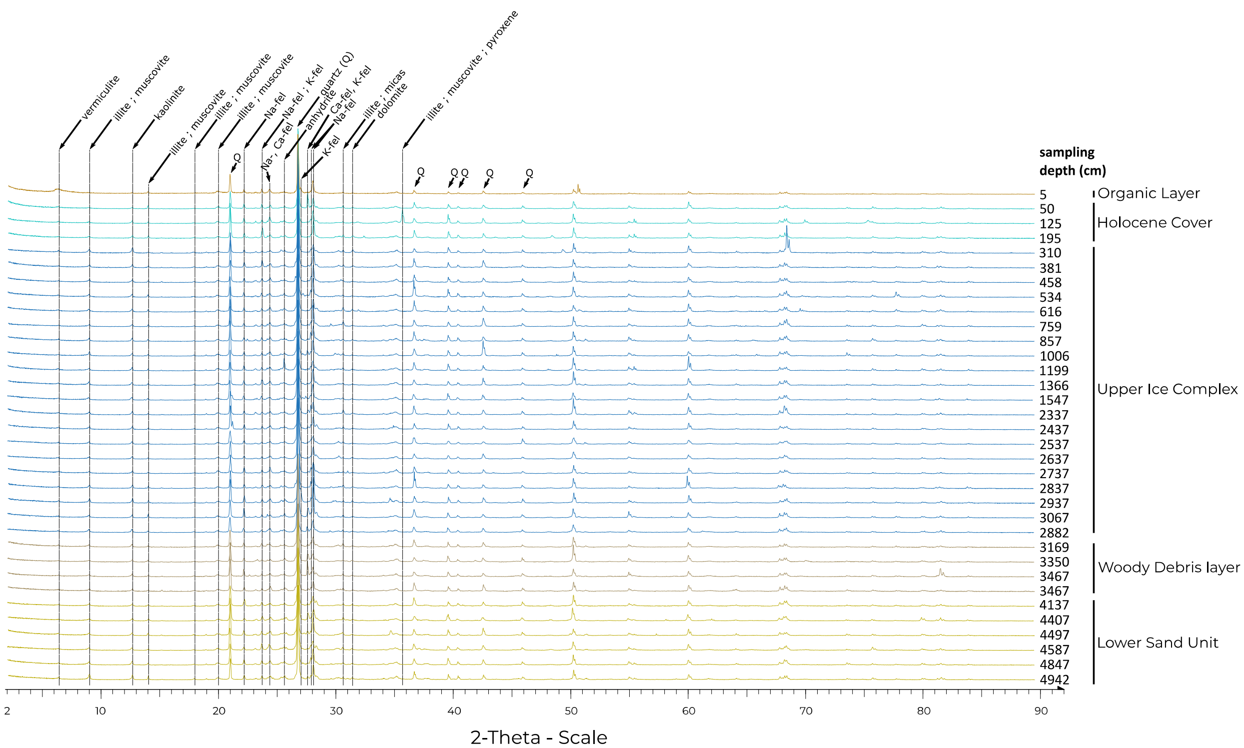

Figure 2 | ***Diffractograms for Batagay thaw slump in sediment profile 1***. *Colors represent the stratigraphic units, namely, from the top to the bottom: the organic layer (OL, n=1, light brown), Holocene Cover (HC, n=3, light blue), Upper Ice Complex (UIC, n = 20, dark blue), Woody Debris layer (WD, n=4, dark brown) and Lower Sand Unit (LSU, n=6, yellow). Q = quartz, fel = feldspar (K-, Na- and Ca-).*

Total calcium (Ca_t) concentrations are significantly higher (p-value < 0.05) in the upper and lower ice complex (UIC and LIC; 5.1 ± 2.1 g/kg) and in the Lower Sand Unit (5.9 ± 1.6 g/kg) than in the younger units (OL and HC; 2.7 ± 0.6 g/kg, **Figure 3**a). For the concentrations in major elements such as iron (Fe) and aluminum (Al), there is no significant difference between Holocene Cover and Woody Debris and units deposited during glacial periods (LIC, LSU & UIC), i.e., 27 ± 3 g/kg for Fe and 62 ± 4 g/kg for Al (**Figure 3**b-c).

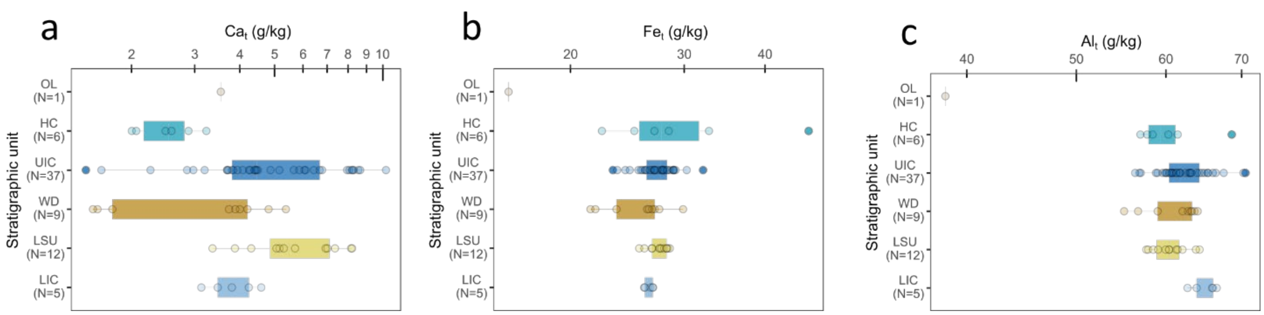

Figure 3 | *Boxplots of* (a) *total calcium (Ca_t),* (b) *total iron (Fe_t) and* (c) *total aluminum (Al_t) concentrations within the stratigraphic units of the Batagay thaw slump, namely, from the top to the bottom: the organic layer (OL), Holocene Cover (HC), Upper Ice Complex (UIC), Woody Debris layer (WD), Lower Sand Unit (LSU) and Lower Ice Complex (LIC). Concentrations are given in g of element per kg of dry matter.*

3.2. Selective mineral elements and organic carbon extractions

Within all profiles, Fe is the dominant metal involved in complexes ($Fe_p/(Fe_p+Al_p+Mn_p)$ = 50 ± 11 % on a molar basis: mmol/kg), followed by Al ($Al_p/(Fe_p+Al_p+Mn_p)$ = 39 ± 7 %) and Mn ($Mn_p/(Fe_p+Al_p+Mn_p)$ = 11 ± 6 %) (see also **Figure S. 5**). The proportion of Fe bound to OC in the form of complexes relative to total Fe (Fe_p/Fe_t) is 3 ± 4 %. This proportion of Fe in the form of complexes is not uniform within the stratigraphic units: the surface organic layer sample reaches 21 %, followed by the Woody Debris layer (6 ± 3 %), the Holocene Cover (4 ± 1 %), the Upper Ice Complex (3 ± 3 %) and finally, the Lower Ice Complex (1.2 ± 0.5 %) and the Lower Sand Unit (0.7 ± 0.3 %).

For Al, the proportion of complexes relative to the total Al is overall much lower than for Fe (Al_p/Al_t = 0.5 ± 0.7 %) and is highest in the shallow organic sample (OL; 4.6 %) followed by the Woody Debris layer (0.7 ± 0.3 %), the Holocene Cover and the Upper Ice Complex (HC and UIC; 0.5 ± 0.4 %) and the deepest units (LSU and LIC; 0.17 ± 0.04 %). For Mn, the proportion of complexes relative to the total Mn (Mn_p/Mn_t) is higher (30 ± 13 %) than for Fe and Al, and is the highest within the organic layer sample (60 %), the lowest within the Holocene Cover samples (9 ± 4 %) and relatively constant within the other units (UIC, WD, LSU, LIC; 31 ± 12 %).

Overall, the sum of metal complexes (Fe_p+Al_p+Mn_p in mmol/kg) is the highest in the organic layer, followed by the Woody Debris layer, in which this sum is significantly higher than in the Holocene Cover and the Upper Ice Complex (p-value < 0.05), in which the sum is significantly higher than in the Lower Sand Unit and the Lower Ice Complex (**Figure S. 5**). When considering the metals most dominant to form complexes with OC individually, Fe is found to explain most of the variability in the C_p distribution (robust linear regression plot between C_p and Fe_p; R^2 adj = 0.82; **Figure S. 6**a), followed by Al_p (R^2 adj = 0.76 ; **Figure S. 6**b) and Mn_p (R^2 adj = 0.49; **Figure S. 6**c). Still, these three metals together provide a better explanation of the distribution of C_p concentrations (R^2 adj = 0.84; **Figure S. 6**d).

The proportion of reactive Fe (Fe_o/Fe_t, i.e., the ratio between the oxalate-extracted Fe concentration and the total Fe concentration) reaches overall 12 ± 8%. It decreases with increasing age of the stratigraphic units (**Figure 4**a): it drops from 33 ± 12% in the organic layer and Holocene Cover samples to 7 ± 2% in the oldest glacial deposit (LIC). The proportion of Fe as poorly crystalline oxides (i.e., $(Fe_o\text{-}Fe_p)/Fe_t$) also decreases (p-value < 0.05) with increasing age of the deposit, from 28 ± 14% for Holocene deposits to 6 ± 2% for Middle Pleistocene deposits (LIC).

Total organic carbon (TOC) content varies within the Batagay headwall, but remains low at 1.2 ± 0.6%, except in the organic layer (OL) where it reaches 15% (**Figure 4**b). With increasing depth, the TOC content reaches a maximum within the Woody Debris layer (1.7 ± 0.5%) and then decreases for the lower ice complex (LIC; 0.7 ± 0.1%). The proportion of TOC forming complexes with metals (C_p/TOC) follows the same general pattern as for the TOC content and represents 29 ± 8 % of the TOC pool but with smaller variations between units (**Figure 4**c). Assuming a maximum sorption capacity of 0.22 g_{OC}/g_{Fe} (Wagai and Mayer, 2007), we can estimate a maximum proportion of 5 ± 4 % of TOC bound to poorly crystalline Fe oxides (Fe_o-Fe_p) within the Batagay headwall. This proportion is highest for the Holocene Cover (19 ± 6 %) and remains significantly lower for all other units (OL; UIC; WD; LSU; LIC; 4 ± 2 %). Lastly, the optical density of oxalate extract (ODOE) is highest for the organic layer (0.365), has the lowest values for the Lower Sand Unit (0.02 ± 0.01) and is intermediate, but more variable, for the other units (HC; UIC; WD; LIC; 0.08 ± 0.05; **Table S. 1**).

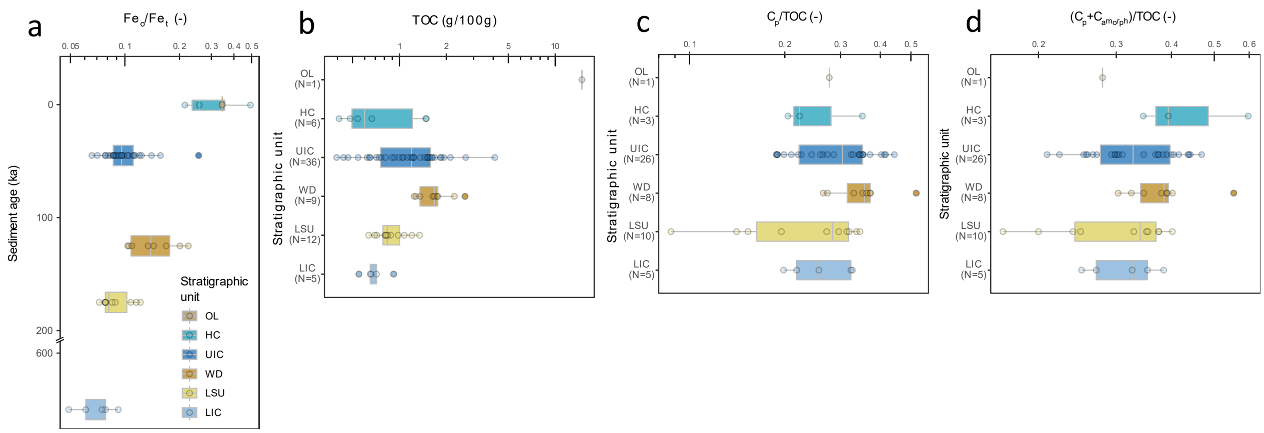

Figure 4 | *Boxplots of* (a) *the ratio oxalate-extracted iron with regard to total iron (Fe_o/Fe_t) as a function of the Batagay sediments depositional age. This Fe either form organo-metallic complexes or associations with OC;* (b-d) *evolution within the stratigraphic units of the Batagay thaw slump of* (b) *total organic carbon (TOC) in sediments,* (c) *pyrophosphate-extracted carbon in regard to total organic carbon (C_p/TOC) in sediments. This refers to the proportion of OC forming complexes with metals;* (d) *sum of proportions of pyrophosphate-extracted carbon and maximum proportion of OC bound to poorly crystalline Fe oxides (($C_p + C_{amorph}$)/TOC) in sediments. This refers to OC that interacts with minerals via complexation with metals or associations to poorly crystalline iron oxides.* *The stratigraphic units of the Batagay thaw slump are, from the top to the bottom: the organic layer (OL), Holocene Cover (HC), Upper Ice Complex (UIC), Woody Debris layer (WD), Lower Sand Unit (LSU) and Lower Ice Complex (LIC). The values of C_{amorph} correspond to a maximum sorption capacity of OC to poorly crystalline Fe oxides (0.22 g_{OC}/g_{Fe} as ferrihydrite). Sediment depositional age as in* ***Table 1****. TOC content is given in g of OC per 100 g of dry matter (wt, %).*

4. Discussion

4.1. Batagay stratigraphic units: similar geological nature but different historical permafrost thaw dynamics

The similar mineral phases found within the different stratigraphic units of the Batagay headwall (**Figure 2**, **Figure S. 3** & **Figure S. 4**) suggest that the geological nature of the source of the sediments did not vary significantly along the depositional period ranging from ~ 650 ka to modern, which is consistent with the formation of deposits involving ice-rich Yedoma (Murton et al., 2015; Schirrmeister et al., 2011; Strauss et al., 2017). The lower Ca_t concentrations in the Holocene Cover and the Woody Debris layers compared to the glacial deposits (LIC, LSU & UIC) (**Figure 3**a) suggest, however, that the conditions for the leaching of more soluble elements such as Ca has not been homogeneous within the period of deposition. The lower Ca_t concentrations likely reflect conditions for a higher leaching of solutes during warmer and/or wetter periods (i.e., HC and WD units). The Woody Debris layer is interpreted as a forest bed supposed to be of last interglacial (MIS 5e) age. It therefore likely experienced warm climate stages (Ashastina et al., 2017; Pisias et al., 1984), with favorable conditions for pedological development. The near-surface Holocene Cover is also characterized by soil formation processes (Murton et al., 2023) and wet depositional conditions are furthermore confirmed by biomarker data (Jongejans et al., 2022a). By contrast, drier depositional conditions especially during the coldest periods are reflected by isotopic and palaeo-ecological analyses in the units representative of the glacial periods (LIC, LSU & UIC) (Ashastina et al., 2018; Opel et al., 2019). This is confirmed by minor variations in the biogeochemical and biomarker parameters for the same units (Jongejans et al., 2022a). From this, it can be inferred that the deposits of the different stratigraphic units of the Batagay thaw slump have a similar source but contrasted conditions of sedimentation, freezing and historical permafrost thaw dynamics.

4.2. Mineral-bound organic carbon in the Batagay megaslump dominated by complexation with metals

Our data demonstrate that the proportion of mineral-bound OC within the headwall of the Batagay megaslump is dominated by the complexation with metals (29 ± 8 % of the TOC; **Figure 4**c) compared to TOC bound to poorly crystalline Fe oxides (5 ± 4 %), with an exception for the Holocene Cover, which has a substantial maximal sorption capacity of OC to amorphous Fe oxides (**Figure 4**c-d). Besides, our measurements of the optical density of oxalate extract (ODOE), representing organic acids forming complexes and adsorbed onto poorly crystalline minerals, show a correlation with the concentration in OC forming complexes with metals (C_p; R^2 adj = 0.7; **Figure 5**a), as well as with the Fe involved in these complexes (Fe_p, **Figure 5**b), but no correlation with the Fe in the form of poorly crystalline Fe oxides (Fe_o-Fe_p, **Figure 5**c) except for the Holocene Cover. This supports that complexation is the dominant mechanism for OC-mineral interactions in the sediments involved in the Batagay thaw slump, except in the Holocene Cover. Totaling the contributions of OC forming complexes with metals (C_p/TOC) and the maximum sorption capacity of OC to poorly crystalline Fe oxides (C_{amorph}/TOC), this results in a maximal total proportion of 34 ± 8 % of the TOC that interacts with either mineral surfaces or mineral elements (**Figure 4**, **Figure S. 7**), with a maximum value for the Holocene Cover (45 ± 13 %) and a minimum value for the Lower Ice Complex (32 ± 6 %).

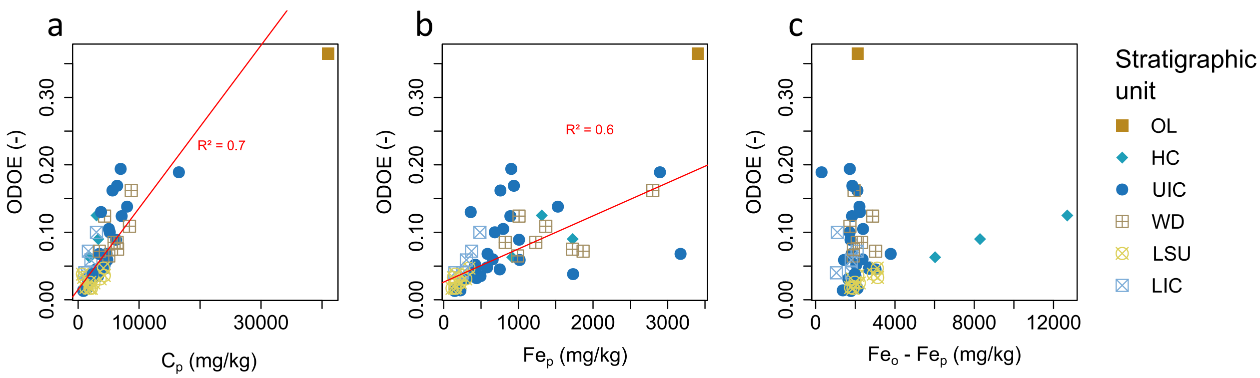

Figure 5 | *Robust linear regression plot between optical density of oxalate extract (ODOE) and (a) pyrophosphate-extracted carbon (C_p), (b) pyrophosphate-extracted iron (Fe_p) and (c) difference between oxalate-extracted iron and pyrophosphate-extracted iron (Fe_o-Fe_p). OL = organic layer, HC = Holocene Cover, UIC = Upper Ice Complex, WD = Woody Debris layer, LSU = Lower Sand Unit and LIC = Lower Ice Complex.*

Apart from the Woody Debris layer, the proportion of OC forming complexes with metals (C_p/TOC) does not vary significantly between stratigraphic units (**Figure 4**c), even though the TOC content differs between units as a function of the environmental conditions at the time of deposition (**Figure 4**b). This is supported by Jongejans et al. (2022a) and references therein. Moreover, the concentration of OC forming complexes with metals (C_p) is proportional to the TOC content (R^2 adj = 0.9; see also supplementary **S5**). This suggests that alternating glacial (with the deposition of LIC, LSU & UIC) and interglacial periods (with the deposition of HC and WD) controls C_p and TOC content to some extent but does not fully control the ratio of OC that forms complexes with metals (C_p/TOC). The homogeneity of the proportion

C_p/TOC within the entire Batagay headwall suggests that metal-organic complexes seem to be stable over time across multiple glacial and interglacial periods. In contrast, OC associations to poorly crystalline Fe oxides seem to be proportionally more limited, and driven by warmer and wetter conditions with the deposition of the Holocene Cover (Ashastina et al., 2017; Jongejans et al., 2022a).

4.3. Interglacial period deposits: mineral-OC interactions and intrinsic chemical composition of OC

From sections **3.2** and **3.2**, we note that the Holocene Cover shows the highest proportion of OC-mineral interactions ((C_p+C_{amorph})/TOC; **Figure 4**d) and that the Woody Debris layer shows the highest concentration of OC forming complexes with metals (C_p), without considering the surface organic layer (see also **Table S. 1**). Biomarker data from samples collected from the same depths (Jongejans et al., 2022a) indicate that the Holocene Cover shows a higher level of degradation and thus a lower quality for organic matter, which makes it therefore less likely to be degraded in the future. Furthermore, high microbial decomposition (favored by higher soil temperatures) within the Woody Debris layer is confirmed by higher-plants fatty acid (HPFA) indexes (Jongejans et al., 2022a). This increased level of microbial transformation of OC and consequent lower quality of organic matter, suggests that further degradation is also unlikely to occur in the future. In contrast, the stratigraphic units corresponding to glacial periods (UIC, LSU, LIC) probably experienced lower microbial activity than the other stratigraphic units (Jongejans et al., 2022a). Consequently, biogeochemical legacy of interglacial periods reveal that the organic matter contained in such units has undergone greater microbial transformation (Jongejans et al., 2022a) and contain a greater proportion of mineral-bound OC. Increased microbiological activity at the time of deposition, combined with warm climate stages and favorable conditions for pedological development turn out to be key factors leading to an OC less likely to contribute to the permafrost-carbon-climate feedback.

4.4. Forms of mineral-OC interactions: comparison across different permafrost sites

In order to position the Batagay sediments within other Arctic regions in terms of organo-mineral interactions, we compared the data from this study with available data from other locations (**Figure 6** & **Figure 7**). It turns out that the pool of mineral-interacting forms of OC in Batagay are comparable to what is found in other thermokarst landforms. More specifically, the comprehensive mineral-interacting proportion of TOC (i.e., via associations with poorly crystalline Fe oxides and in complexed form; (C_p+C_{amorph})/TOC) from Batagay is (i) in line with the literature for both drained thaw lake basins in northern Alaska (Mueller et al., 2015) and slump deformations in the Qinghai-Tibetan Plateau (Mu et al., 2020), as for Peel Plateau (Canada) thaw slumps (Thomas et al., 2023), circum-Arctic Yedoma sediments (Monhonval et al., 2021b) and lowland thermokarst landscape in Eight Mile Lake, Alaska (Monhonval et al., 2023), (ii) higher than in palsa (Patzner et al., 2020) and in marine sediments from the Eurasian Arctic Shelf (Salvadó et al., 2015), and (iii) in the low range compared to Yedoma from the Bol'shoy Lyakhovsky Island (Martens et al., 2023) and soils from the Lower Kolyma Region (Gentsch et al., 2015; Figure 6; Table S. 2) and significantly lower than Yedoma permafrost in northeastern Siberia (Dutta et al., 2006). The active layer (and generally the surface organic layers) appear to have a lower proportion of mineral-interacting OC than in the less TOC-rich permafrost layers (Gentsch et al., 2015; Monhonval et al., 2023). This could be attributed to a relative OC oversaturation in regard the mineral surfaces or elements available for mineral-OC interactions in the superficial layers and possible inputs of modern labile OC from actively growing plants. This is also observed in palsa (sampling depths < 25 cm in Patzner et al., 2020) and in superficial sediment samples from the Eurasian Arctic Shelf (Salvadó et al., 2015). The proportions of mineral-bound OC in Yedoma sediments (refs Dutta et al., 2006; Martens et al., 2023; Monhonval et al., 2021b) are highly variable between sites. It can be argued that this results from the polygenetic origin of Yedoma deposits, with seasonally differentiated deposition mechanisms controlled by local environmental conditions, including the contribution from local fluvial, colluvial, and alluvial sediments (Schirrmeister et al., 2020, 2013; Strauss et al., 2013).

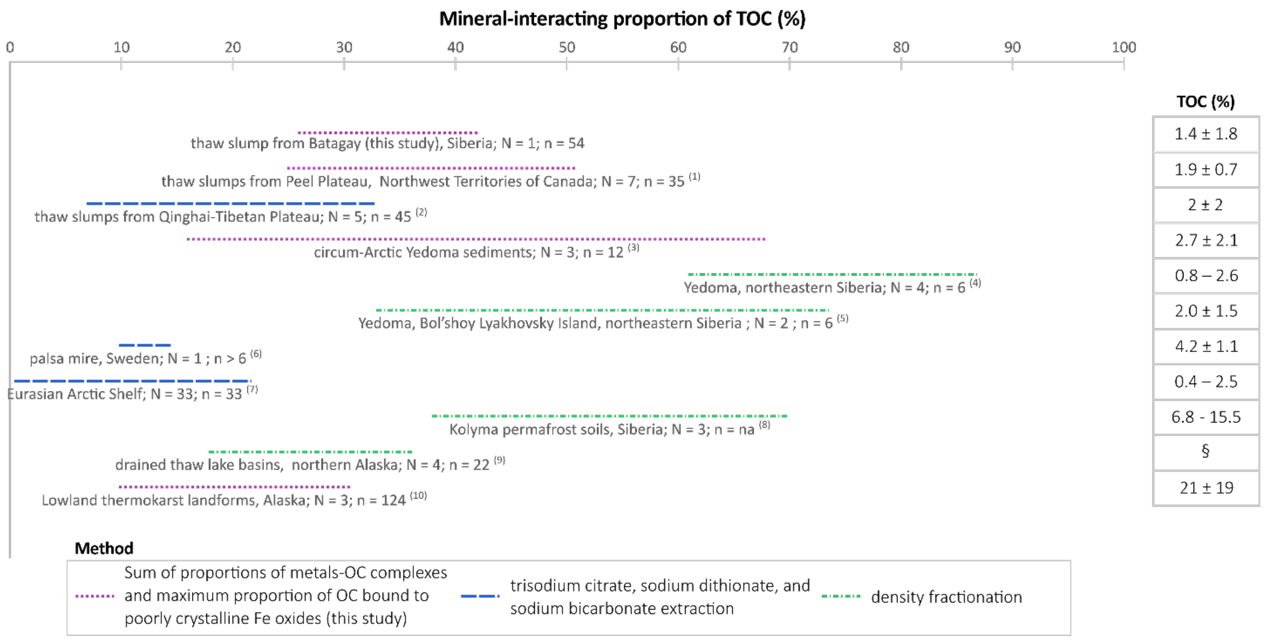

Figure 6 | *Comparison of mineral-interacting forms of OC in the entire headwall of the Batagay thaw slump, with other contrasting deposits throughout the Arctic. The percentages are given on a mass basis. Three different methods have been used: the sum of proportions of metals-OC complexes and maximum proportion of OC bound to poorly crystalline Fe oxides as in this study (purple); trisodium citrate, sodium dithionate, and sodium bicarbonate extraction from Lalonde et al. (2012), Mehra and Jackson (1958), Poulton and Canfield (2005) (blue) ; and density fractionation method with sodium polytungstate in Dutta et al. (2006), Gentsch et al. (2015), Mueller et al. (2015) (green). §OC expressed in stock: 54 ± 15 kg/m^{-3}. N = number of sites/cores; n = number of samples. na = not available.* *(1) Thomas et al. (2023); (2) Mu et al. (2020); (3) Monhonval et al. (2021b); (4) Dutta et al. (2006); (5) Martens et al. (2023) ; (6) Patzner et al. (2020); (7) Salvadó et al. (2015); (8) Gentsch et al. (2015); (9) Mueller et al. (2015); (10) Monhonval et al. (2023);*

Beyond the numerical results, we acknowledge that the method for obtaining a comprehensive assessment of mineral-interacting proportion of TOC does not appear to be a critical factor. More specifically, the method used in this study, or the trisodium citrate, sodium dithionate, and sodium bicarbonate extraction method (Lalonde et al., 2012; Mehra and Jackson, 1958; Poulton and Canfield, 2005) or even the density fractionation method with sodium polytungstate, does not appear to give results that are systematically biased in either direction (**Figure 6**).

Where possible, we compared the mechanisms involved in OC-mineral interactions, i.e., complexation or associations with poorly crystalline Fe oxides. In ice-rich sediments (**Figure 7**a), the proportions of OC forming complexes with metals are comparable, but the potential for association with poorly crystalline Fe oxides is more variable. More specifically, pyrophosphate-extracted carbon (C_p) concentrations are in the same range between (i) the two ice complex units in Batagay (UIC - or Yedoma - and LIC), (ii) circum-Arctic Yedoma sediments (Monhonval et al., 2021b), (iii) undisturbed Yedoma in Yukechi (Monhonval et al., 2022) and (iv) Pleistocene-aged ice-rich tills in the Peel Plateau (Thomas et al., 2023), even though there is more variability in the Yedoma at the Arctic scale (**Table S. 3**). The proportion of OC in the form of complexes with metals (C_p/TOC; **Figure 7**a; **Table S. 3**) is also similar for the different studies. The maximum sorption capacity of the OC to poorly crystalline Fe oxides (C_{amorph}/TOC), on the other hand, shows more variability between sites, with higher values within the Pleistocene-aged ice-rich tills in the Peel Plateau compared to the Lower Ice Complex and Upper Ice Complex (Yedoma) deposits in Batagay. This also applies for reactive Fe (Fe_o) concentrations and the proportion of reactive Fe to total Fe (Fe_o/Fe_t), (**Table S. 3**).

We also compared sediments from interglacial periods with other locations (**Figure 7**b). This supports the argument that wet depositional conditions, warm climate stages and pedological development appear to be key conditions for a highest potential for OC association with poorly crystalline Fe oxides. Furthermore, this seems to be applicable beyond a single site. Specifically, that maximal proportion of OC sorbed to poorly crystalline Fe oxides (C_{amorph}/TOC) is significantly higher in the Batagay Holocene Cover (HC) than in (i) all other units of the Batagay thaw slump headwall; (ii) circum-Arctic Yedoma sediments (Monhonval et al., 2021b) and (iii) permafrost soils in lowland thermokarst landforms (Monhonval et al., 2023) (**Figure 7**a). The Holocene Cover at Batagay is otherwise comparable with Holocene-modified deposits in the Peel Plateau that experienced past thaw during the Holocene thermal maximum (Thomas et al., 2023; **Figure 7**b), while falling within the upper range compared to Pleistocene-aged ice-rich tills in the Peel Plateau (**Figure 7**a).

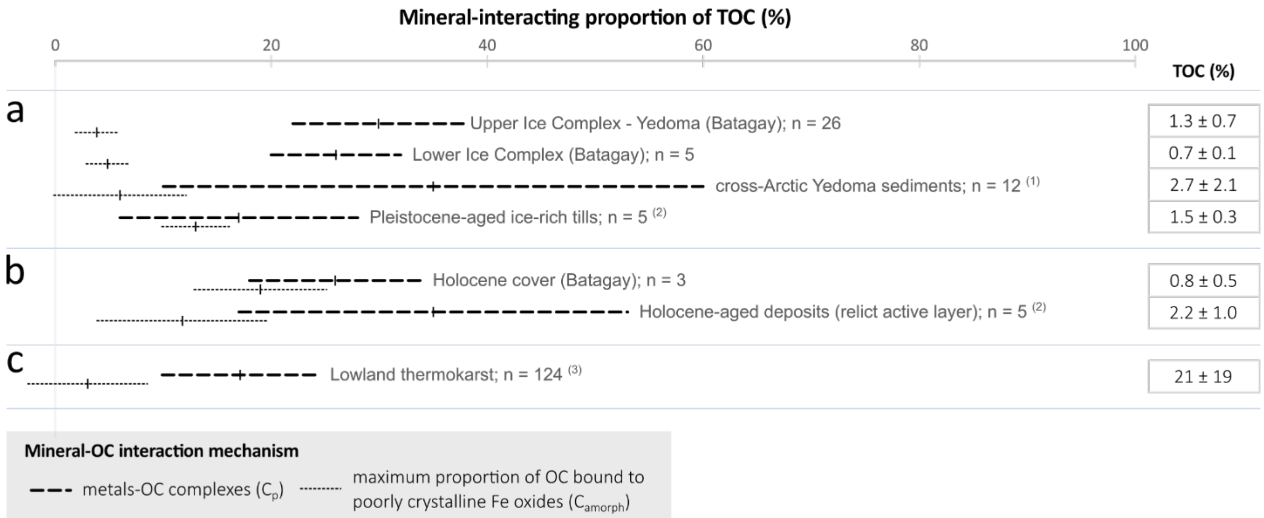

Figure 7 | *Comparison of mineral-interacting forms of OC in the Upper Ice Complex (UIC), Lower Ice Complex (LIC) and Holocene Cover (HC) units within the Batagay thaw slump, with other similar deposits throughout the Arctic. (a) ice-rich sediments; (b) sediments from interglacial periods; (c) sediments from lowland thermokarst landforms. We used the maximum sorption capacity of OC to poorly crystalline Fe oxides (0.22 g_{OC}/g_{Fe} as ferrihydrite). The percentages are given on a mass basis. The distributions are represented by the mean ± standard deviation. [(1)] circum-Arctic Yedoma sediments (Monhonval et al., 2021b); [(2)]Layers from thaw slump headwalls from the Peel Plateau, western canadian Arctic (Thomas et al., 2023); [(3)]Eight Mile Lake, Central Alaska (Monhonval et al., 2023)*

When comparing the Batagay thaw slump (entire headwall; Figure 7a-b) with lowland thermokarst landforms (Monhonval et al., 2023; Figure 7c), the pyrophosphate-extracted carbon (C_p) and TOC content at Batagay are in the low range of values found in region of lowland thermokarst degradation, but the complexed fraction relative to the total (C_p/TOC) is in the same range (Table S. 2). Overall, this suggests that OC-metal complexation is the dominant mechanism within the mineral-interacting forms of OC, regardless of the sampling location.

4.5. Interglacial period deposits: only 25% of the OC mass mobilized from the sediments of the Batagay thaw slump

Using the sampling depths along the headwall and an estimate of the headwall retreat rate (Vadakkedath et al., 2020), we established a first order estimate of ~10^6 m³ of total volume retreated annually from the Batagay collapse front (on average, between 1991 and 2018). This volume estimate is in line with Günther et al. (2015) who derived a total thawed volume of 2.4×10^7 m³ through 2014, i.e., ~0.7×10^6 m³/year, assuming that the second stage of the disturbance (i.e., causing rapid thermo-denudational development of the thaw slump; Murton et al., 2023) started at the end of the 1980s. Using the bulk density of the sediments and TOC content on the profile, we were able to establish an estimate of ~ 1.2×10^7 kg of OC mobilized annually from the Batagay thaw slump (**Figure 8**a). Beyond the absolute value of this mobilized mass, this reveals that the units deposited during the glacial periods (i.e., UIC, LSU and LIC), together represent 72% of the OC mass mobilized from the Batagay thaw slump. We note that deposits from interglacial periods account jointly ~ 25% of the OC mobilized from the slump, even though they resulted in a greater proportion of the mineral-bound OC pool. In relative terms, the units that show the greater portion of OC within the Batagay slump headwall therefore do not contribute much to the total mass of OC mobilized by the collapsing feature.

The OC flux estimate is subject to significant uncertainties. First, it was not possible to consider the Upper Sand Unit in the calculation, as it was not sampled in this study. After estimation based on Kizyakov et al. (2023) the Upper Sand Unit, however, only represents a vertical surface area of about 2% of the headwall (based on the structure of the western part of the RTS vertical headwall). We acknowledge that more downslope and across all former headwalls, the Upper Sand Unit could potentially represent about 15 m in thickness (Opel et al., 2019). Additionally, the stratigraphic units do not have a uniform thickness along the headwall. For instance, the exposed thickness of the Lower Sand Unit decreases to ~zero in the northwestern part of the central headwall (while the thickness of the Upper Ice Complex increases). Yet, it can be seen within Kizyakov et al. (2023) that, overall, the stratigraphic units that have the largest mass balance contribution (UIC and LSU) have thicknesses that do not vary for more than 4 m for the UIC and 8 m for the LSU (based on 2019 field observation within observed headwalls). For the UIC, an additional 4 m thick contribution represents a potential increase in the volume estimate of 0.1×10^6 m³/yr and ~0.01×10^7 kg/yr (1%) increase in TOC mobilization, based on the *average* TOC content for this unit. Similarly, 8 m thicker LSU for the entire headwall would represent an increase in 3% of TOC mobilization. Finally, headwall height is not uniform throughout the collapse front. All these considerations imply that the flux estimate presented in this study should be considered as a first order estimate, which is not intended to be more accurate than within an order of magnitude. Another point to note is that this mass balance does not take into account the dissolved organic carbon (DOC) that may be present in ice wedges. According to Fritz et al. (2015), who analyzed different ice bodies throughout the Arctic, ice wedges could contain up to 28.6 mg/L of DOC. For the Batagay slump, Kizyakov et al. (2024) found a mean ice wedge DOC content of 19 mg/L as a first estimate based on 47 samples. If we extrapolate this concentration to the entire volume of ice exported by the Batagay megaslump annually, we obtain a first order estimate of 10^4 kg of DOC per year, which is three orders of magnitude lower than the mass of TOC exported by the sediments. If we consider comparatively higher concentrations of DOC for the pore ice in the sediments, i.e. a mean of to 560 mg/L (Kizyakov et al., 2024) and carry out the same extrapolation procedure, we obtain 3×10^5 kg DOC per year exported by the ice, which corresponds to 2 % of the OC exported by the sediments. Even so, we recognize that DOC, although not representing a substantial part of the mass balance, is still of major importance for biogeochemical processes, being potentially highly labile compared to sediment TOC (Vonk et al., 2013a, 2013b, 2012). When comparing the mass of OC mobilized by the Batagay thaw slump to the masses mobilized by megaslumps[1] from the Peel Plateau in Canada (Thomas et al., 2023), it appears that the mass of OC mobilized by the Batagay thaw slump is ~7 times greater than that mobilized by that of the slump FM2 and ~65 times greater than that mobilized by slump FM3 (Figure 8b). Yet, slump FM3 at the Peel Plateau is already qualified as a mega-slump and still mobilizes ~65 times less OC than Batagay. We note that a portion of the debris mobilized by the Batagay thaw slump can potentially refreeze after headwall erosion and burial in the slumped zone, resulting in permafrost re-establishment in the scar zone as the slump stabilizes (Burn and Friele, 1989; Kokelj et al., 2009). In Batagay however, there is a clear predominance of the erosion process (removal of material and deepening of the channel), which is evidenced by a narrow erosional valley with a V-shaped transverse profile. Yet, it is not expected that all of the debris would be effectively exposed to thaw after slump-induced mobilization of material. Further studies are needed to quantify the full image of C flux, including losses as gas and the particulate proportion that stabilizes locally and refreezes, out of which a portion forms a new active-layer within the scar zone.

[1] FM2 headwall height = 18.6 m and scar zone area = 32.7 ha ; FM3 headwall height = 6.5 m and scar zone area = 6.7 ha (Thomas et al., 2023 and references therein)

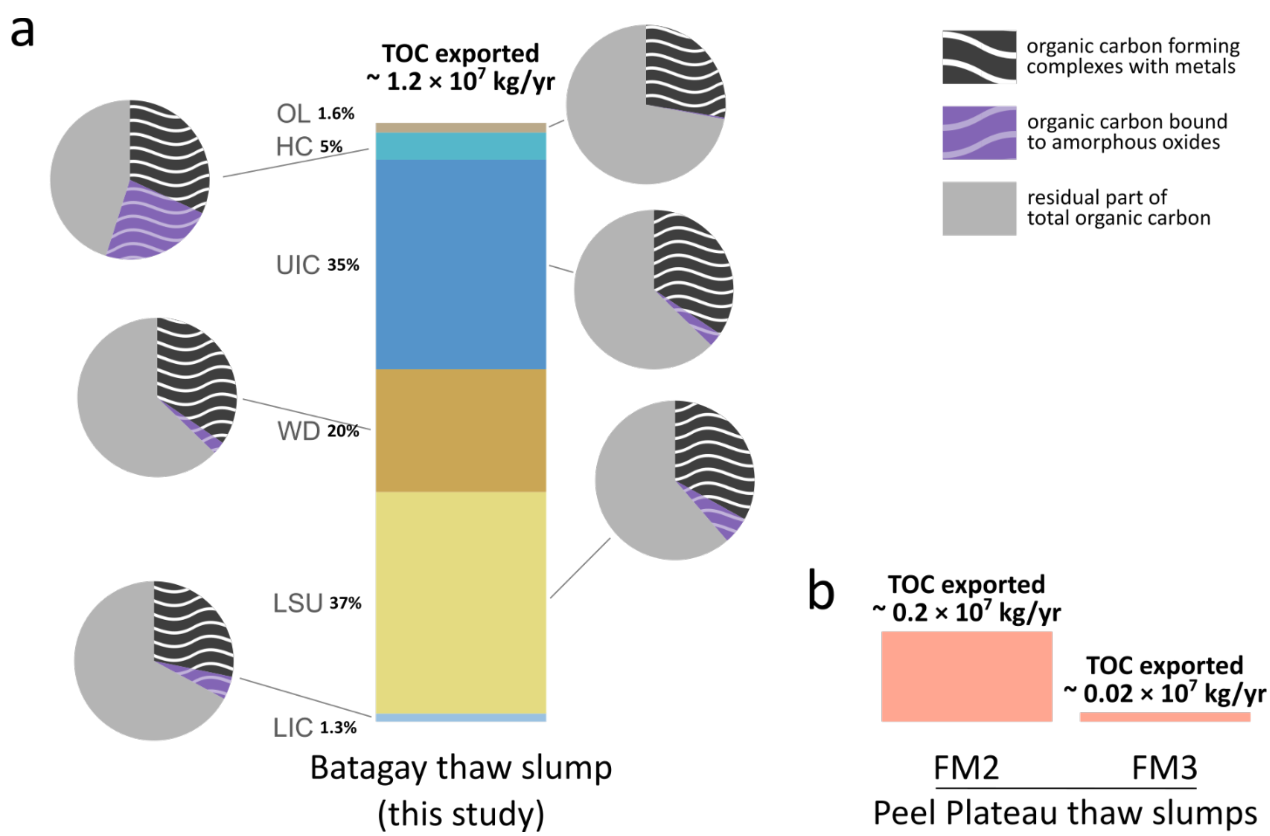

Figure 8 | *Annual mass balance assessment of the sediment material eroded by the retreat of the collapse front of the Batagay thaw slump in comparison to Peel Plateau thaw slumps. a) Batagay thaw slump displaced material mass distribution modeling within the different stratigraphic units (bar-plot) & mass proportion of mineral-interacting forms of organic carbon within the units (pie-charts). OL = organic layer, HC = Holocene Cover, UIC = Upper Ice Complex, WD = Woody Debris layer, LSU = Lower Sand Unit and LIC = Lower Ice Complex (LIC) with color codes following Fig. 2-5.; b) Comparison with Peel Plateau thaw slumps FM2 and FM3 (data from Thomas et al., 2023). TOC = total organic carbon*

5. Conclusions

We studied the mechanism for OC-mineral interactions within the Batagay megaslump, the largest known thaw slump headwall exposing the second oldest directly dated permafrost in the Northern Hemisphere. We compared our results with available data from other locations in the Arctic and established a first order estimate of the mass of material eroded annually by the retreat of the collapse front, along with an overall assessment of the OC-mineral interactions within this mobilized material. In conclusion, we found that:

(i) Deposits of the Batagay stratigraphic units have a similar geological nature but different historical permafrost thaw dynamics.

(ii) Within the Batagay headwall, complexation is the dominant mechanism for OC-mineral interactions in the sediments and represents 29 ± 8 % of the TOC, while we estimate a maximal proportion of 5 ± 4 % of the TOC involved in OC-Fe oxide associations. We estimate accordingly that the combination of the two mechanisms results in 34 ± 8 % of the TOC pool that interacts with mineral surfaces or elements.

(iii) The forms and proportion of OC-mineral interactions at Batagay are in the same range quantitatively, compared to those found in other hillslope thermokarst landforms.

(iv) Batagay sediments from interglacial periods show higher OC-mineral interactions, along with organic matter that has undergone more microbial transformation and is therefore presumably less biodegradable. Yet, such units account jointly for ~ 25% of the OC mass mobilized from the Batagay thaw slump.

(v) We provide a first order estimate of ~ 1.2×10^7 kg of OC mobilized annually downslope of the headwall, with a maximum of 38% interacting with mineral element or surfaces by complexation with metals or associations to poorly crystalline iron oxides.

These data support that more than one third of the TOC exposed by this massive thaw slump is not directly available for mineralization, but rather interacting with the mineral fraction of the sediments.

Author contributions

MT and SO conceived and planned the experimental work. CV and SC realized most of the experimental work under the supervision and with the help of MT. AK, LJ, SW and TO and conducted the field work. LJ provided data on total organic carbon concentrations and bulk density. LJ, JS, AK, TO, SW and GG contributed with their expertise on the study area. MT wrote the manuscript under the supervision of SO with inputs from all co-authors.

Funding

This project received funding from the European Union’s Horizon 2020 research and innovation program under grant agreement No.714617 to SO (WeThaw), and SO acknowledges funding from the Fund for Scientific Research FNRS in Belgium (FC69480). Further funding for this work came from the Leverhulme Trust (Research Project Grant RPG-2020-334) and the AWI baseline funds for the expedition Batagay 2019. LJ acknowledges the German Federal Environmental Foundation (DBU; project name: “Organic matter stored in ice-rich permafrost: future permafrost thaw and greenhouse gas release”).

Declaration of Competing Interest

The authors declare that they have no known competing financial interests or personal relationships that could have appeared to influence the work reported in this paper.

Acknowledgments

The authors acknowledge fieldwork support from Dmitry Ukhin, Hanno Meyer, Jeremy Courtin, Igor Syromyatnikov, and Andrei Shepelev. The authors further acknowledge Laurence Monin, Claudine Givron, Élodie Devos, and Hélène Dailly from the Mineral and Organic Chemical Analysis (MOCA) platform at UCLouvain for conducting chemical analysis, and Arthur Monhonval, Catherine Hirst, and all the members of the WeThaw project for useful discussions. MT thanks the members of the ELIE-SOIL lab for useful critical comments.

Data availability statement

All data are made available as supplement to the paper.

References

Abbott, B.W., Jones, J.B., 2015. Permafrost collapse alters soil carbon stocks, respiration, CH4, and N2O in upland tundra. Global Change Biology 21, 4570–4587. https://doi.org/10.1111/gcb.13069

Ashastina, K., Kuzmina, S., Rudaya, N., Troeva, E., Schoch, W.H., Römermann, C., Reinecke, J., Otte, V., Savvinov, G., Wesche, K., Kienast, F., 2018. Woodlands and steppes: Pleistocene vegetation in Yakutia's most continental part recorded in the Batagay permafrost sequence. Quaternary Science Reviews 196, 38–61. https://doi.org/10.1016/j.quascirev.2018.07.032

Ashastina, K., Schirrmeister, L., Fuchs, M., Kienast, F., 2017. Palaeoclimate characteristics in interior Siberia of MIS 6–2: first insights from the Batagay permafrost mega-thaw slump in the Yana Highlands. Climate of the Past 13, 795–818. https://doi.org/10.5194/cp-13-795-2017

Bascomb, C.L., 1968. Distribution of Pyrophosphate-Extractable Iron and Organic Carbon in Soils of Various Groups. Journal of Soil Science 19, 251–268. https://doi.org/10.1111/j.1365-2389.1968.tb01538.x

Blakemore, L.C., Searle, P.L., Daly, B.K., 1981. Methods for chemical analysis of soils. New Zealand Soil Bur. Scientific Rep., second revision 10A. https://doi.org/10.7931/DL1-SBSR-10A

Bröder, L., Hirst, C., Opfergelt, S., Thomas, M., Vonk, J.E., Haghipour, N., Eglinton, T.I., Fouché, J., 2022. Contrasting Export of Particulate Organic Carbon From Greenlandic Glacial and Nonglacial Streams. Geophysical Research Letters 49, e2022GL101210. https://doi.org/10.1029/2022GL101210

Brooker, A., Fraser, R.H., Olthof, I., Kokelj, S.V., Lacelle, D., 2014. Mapping the Activity and Evolution of Retrogressive Thaw Slumps by Tasselled Cap Trend Analysis of a Landsat Satellite Image Stack. Permafrost and Periglacial Processes 25, 243–256. https://doi.org/10.1002/ppp.1819

Burn, C.R., Friele, P.A., 1989. Geomorphology, Vegetation Succession, Soil Characteristics and Permafrost in Retrogressive Thaw Slumps near Mayo, Yukon Territory. Arctic 42, 31–40.

Burn, C.R., Lewkowicz, A.G., 1990. Canadian Landform Examples - Retrogressive Thaw Slumps. Can. Geogr. 34, 273–276. https://doi.org/10.1111/j.1541-0064.1990.tb01092.x

Courchesne, F., Turmel, M.-C., 2008. Extractable Al, Fe, Mn, and Si, in: Carter, M.R., Gregorich, E.G (Eds.), Soil Sampling and Methods of Analysis. Canadian Society of Soil Science ; CRC Press, [Pinawa, Manitoba] : Boca Raton, FL, pp. 307–315.

Daly, B.K., 1982. Identification of podzols and podzolised soils in New Zealand by relative absorbance of oxalate extracts of A and B horizons. Geoderma 28, 29–38. https://doi.org/10.1016/0016-7061(82)90038-6

Dobricic, S., Pozzoli, L., 2019. Arctic permafrost thawing: impacts on high latitude emissions of carbon dioxide and methane. Publications Office of the European Union, LU.

Dutta, K., Schuur, E. a. G., Neff, J.C., Zimov, S.A., 2006. Potential carbon release from permafrost soils of Northeastern Siberia. Global Change Biology 12, 2336–2351. https://doi.org/10.1111/j.1365-2486.2006.01259.x

Fox-Kemper, B., Hewitt, H.T., Xiao, C., Aðalgeirsdóttir, G., Drijfhout, S.S., Edwards, T.L., Golledge, N.R., Hemer, M., Koop, R.E., Krinner, G., Mix, A., Notz, D., Nowicki, S., Nurhati, I.S., Ruiz, L., Sallée, J.-B., Slangen, A.B.A., Yu, Y., 2021. Ocean, Cryosphere and Sea Level Change, in: Masson-Delmotte, V., Zhai, P., Pirani, A., Connors, S.L., Péan, C., Berger, S., Caud, N., Chen, Y., Goldfarb, L., Gomis, M.I., Huang, M., Leitzell, K., Lonnoy, E., Matthews, J.B.R., Maycock, T.K., Waterfield, T., Yelekçi, O., Yu, R., Zhou, B. (Eds.), Climate Change 2021: The Physical Science Basis. Contribution of Working Group I to the Sixth Assessment Report of the Intergovernmental Panel on Climate Change. Cambridge University Press, Cambridge, United Kingdom and New York, NY, USA, pp. 1211–1362. https://doi.org/10.1017/9781009157896.011

Fritz, M., Opel, T., Tanski, G., Herzschuh, U., Meyer, H., Eulenburg, A., Lantuit, H., 2015. Dissolved organic carbon (DOC) in Arctic ground ice. The Cryosphere 9, 737–752. https://doi.org/10.5194/tc-9-737-2015

García-Palacios, P., Bradford, M.A., Benavente-Ferraces, I., de Celis, M., Delgado-Baquerizo, M., García-Gil, J.C., Gaitán, J.J., Goñi-Urtiaga, A., Mueller, C.W., Panettieri, M., Rey, A., Sáez-Sandino, T., Schuur, E.A.G., Sokol, N.W., Tedersoo, L., Plaza, C., 2024. Dominance of particulate organic carbon in top mineral soils in cold regions. Nat. Geosci. 1–6. https://doi.org/10.1038/s41561-023-01354-5

Gentsch, N., Mikutta, R., Shibistova, O., Wild, B., Schnecker, J., Richter, A., Urich, T., Gittel, A., Šantrůčková, H., Bárta, J., Lashchinskiy, N., Mueller, C.W., Fuß, R., Guggenberger, G., 2015. Properties and bioavailability of particulate and mineral-associated organic matter in Arctic permafrost soils, Lower Kolyma Region, Russia. European Journal of Soil Science 66, 722–734. https://doi.org/10.1111/ejss.12269

Günther, F., Grosse, G., Wetterich, S., Jones, B.M., Kunitsky, V.V., Kienast, F., Schirrmeister, L., 2015. The Batagay mega thaw slump, Yana Uplands, Yakutia, Russia: permafrost thaw dynamics on decadal time scale, in: EPIC3PAST Gateways - Palaeo-Arctic Spatial and Temporal Gateways - Third International Conference and Workshop, Potsdam, Germany, 2015-05-18-2015-05-22Potsdam, TERRA NOSTRA - Schriften Der GeoUnion Alfred-Wegener-Stiftung. Presented at the PAST Gateways - Palaeo-Arctic Spatial and Temporal Gateways - Third International Conference and Workshop, TERRA NOSTRA - Schriften der GeoUnion Alfred-Wegener-Stiftung, Potsdam.

Heginbottom, J.A., Brown, J., Humlum, O., Svensson, H., 2012. Permafrost and Periglacial Environments, in: State of the Earth's Cryosphere at the Beginning of the 21st Century : Glaciers, Global Snow Cover, Floating Ice, and Permafrost and Periglacial Environments, USGS 1386 Series Professional Paper. U.S. Geological Survey, Reston, VA, pp. A425–A496.

Hintze, J.L., Nelson, R.D., 1998. Violin Plots: A Box Plot-Density Trace Synergism. The American Statistician 52, 181. https://doi.org/10.2307/2685478

Hugelius, G., Strauss, J., Zubrzycki, S., Harden, J.W., Schuur, E. a. G., Ping, C.-L., Schirrmeister, L., Grosse, G., Michaelson, G.J., Koven, C.D., O'Donnell, J.A., Elberling, B., Mishra, U., Camill, P., Yu, Z., Palmtag, J., Kuhry, P., 2014. Estimated stocks of circumpolar permafrost carbon with quantified uncertainty ranges and identified data gaps. Biogeosciences 11, 6573–6593. https://doi.org/10.5194/bg-11-6573-2014

IPCC, 2019. IPCC Special Report on the Ocean and Cryosphere in a Changing Climate: Summary for Policymakers., in: Pörtner, H.-O., Roberts, D.C., Masson-Delmotte, V., Zhai, P., Tignor, M., Poloczanska, E., Mintenbeck, K., Nicolai, M., Okem, A., Petzold, J., Rama, B., Weyer, N. (Eds.), .

Jeanroy, E., Guillet, B., 1981. The occurrence of suspended ferruginous particles in pyrophosphate extracts of some soil horizons. Geoderma 26, 95–105. https://doi.org/10.1016/0016-7061(81)90078-1

Jongejans, L.L., Mangelsdorf, K., Karger, C., Opel, T., Wetterich, S., Courtin, J., Meyer, H., Kizyakov, A.I., Grosse, G., Shepelev, A.G., Syromyatnikov, I.I., Fedorov, A.N., Strauss, J., 2022a. Molecular biomarkers in Batagay megaslump permafrost deposits reveal clear differences in organic matter preservation between glacial and interglacial periods. The Cryosphere 16, 3601–3617. https://doi.org/10.5194/tc-16-3601-2022

Jongejans, L.L., Mangelsdorf, K., Karger, C., Strauss, J., 2022b. Total (organic) carbon and nitrogen content in ancient permafrost deposits at the Batagay Megaslump, East Siberia. In: Jongejans, LL et al. (2022): Alkane, fatty acid, total (organic) carbon and nitrogen distribution in ancient permafrost deposits at the Batagay Megaslump, East Siberia. PANGAEA, https://doi.org/10.1594/PANGAEA.950124. https://doi.org/10.1594/PANGAEA.949658

Jongejans, L.L., Opel, T., Courtin, J., Meyer, H., Kizyakov, A., Syromyatnikov, I., Shepelev, A., Wetterich, S., Fedorov, A., Kruse, S., 2021. Batagay outcrop sampling, in: Fuchs, M., Bolshiyanov, D., Grigoriev, M., Morgenstern, A., Pestryakova, L., Tsibizov, L., Dill, A. (Eds.), Russian-German Cooperation: Expeditions to Siberia in 2019, Reports on Polar and Marine Research. Alfred Wegener Institute for Polar and Marine Research, Bremerhaven, Germany, pp. 155–210.

Kaiser, K., Zech, W., 1996. Defects in estimation of aluminum in humus complexes of podzolic soils by pyrophosphate extraction. Soil science 161, 452–458. https://doi.org/10.1097/00010694-199607000-00005

Keil, R.G., Mayer, L.M., 2014. Mineral Matrices and Organic Matter, in: Holland, H.D., Turekian, K.K. (Eds.), Treatise on Geochemistry (Second Edition). Elsevier, Oxford, pp. 337–359. https://doi.org/10.1016/B978-0-08-095975-7.01024-X

Kizyakov, A.I., Korotaev, M.V., Wetterich, S., Opel, T., Pravikova, N.V., Fritz, M., Lupachev, A.V., Günther, F., Shepelev, A.G., Syromyatnikov, I.I., Fedorov, A.N., Zimin, M.V., Grosse, G., 2024. Characterizing Batagay megaslump topography dynamics and matter fluxes at high spatial resolution using a multidisciplinary approach of permafrost field observations, remote sensing and 3D geological modeling. Geomorphology 109183. https://doi.org/10.1016/j.geomorph.2024.109183

Kizyakov, A.I., Wetterich, S., Günther, F., Opel, T., Jongejans, L.L., Courtin, J., Meyer, H., Shepelev, A.G., Syromyatnikov, I.I., Fedorov, A.N., Zimin, M.V., Grosse, G., 2023. Landforms and degradation pattern of the Batagay thaw slump, Northeastern Siberia. Geomorphology 420, 108501. https://doi.org/10.1016/j.geomorph.2022.108501

Kleber, M., Eusterhues, K., Keiluweit, M., Mikutta, C., Mikutta, R., Nico, P.S., 2015. Mineral–Organic Associations: Formation, Properties, and Relevance in Soil Environments, in: Sparks, D.L. (Ed.), Advances in Agronomy. Academic Press, pp. 1–140. https://doi.org/10.1016/bs.agron.2014.10.005

Kögel-Knabner, I., Guggenberger, G., Kleber, M., Kandeler, E., Kalbitz, K., Scheu, S., Eusterhues, K., Leinweber, P., 2008. Organo-mineral associations in temperate soils: Integrating biology, mineralogy, and organic matter chemistry. Journal of Plant Nutrition and Soil Science 171, 61–82. https://doi.org/10.1002/jpln.200700048

Kokelj, S.V., Jorgenson, M.T., 2013. Advances in Thermokarst Research. Permafrost and Periglacial Processes 24, 108–119. https://doi.org/10.1002/ppp.1779

Kokelj, S.V., Kokoszka, J., van der Sluijs, J., Rudy, A.C.A., Tunnicliffe, J., Shakil, S., Tank, S.E., Zolkos, S., 2021. Thaw-driven mass wasting couples slopes with downstream systems, and effects propagate through Arctic drainage networks. The Cryosphere 15, 3059–3081. https://doi.org/10.5194/tc-15-3059-2021

Kokelj, S.V., Lantz, T.C., Kanigan, J., Smith, S.L., Coutts, R., 2009. Origin and polycyclic behaviour of tundra thaw slumps, Mackenzie Delta region, Northwest Territories, Canada. Permafrost and Periglacial Processes 20, 173–184. https://doi.org/10.1002/ppp.642

Kokelj, S.V., Tunnicliffe, J., Lacelle, D., Lantz, T., Fraser, R., 2015a. Retrogressive thaw slumps: From slope process to the landscape sensitivity of northwestern Canada. Presented at the GeoQuebec 2015 Conference, Quebec City, Quebec, Canada.

Kokelj, S.V., Tunnicliffe, J., Lacelle, D., Lantz, T.C., Chin, K.S., Fraser, R., 2015b. Increased precipitation drives mega slump development and destabilization of ice-rich permafrost terrain, northwestern

Canada. Global and Planetary Change 129, 56–68. https://doi.org/10.1016/j.gloplacha.2015.02.008

Kokelj, S.V., Tunnicliffe, J.F., Lacelle, D., 2016. Landscapes and Landforms of Western Canada. https://doi.org/10.1007/978-3-319-44595-3_7

Köppen, W., 1884. Die Wärmezonen der Erde, nach der Dauer der heissen, gemässigten und kalten Zeit und nach der Wirkung der Wärme auf die organische Welt betrachtet (The thermal zones of the earth according to the duration of hot, moderate and cold periods and to the impact of heat on the organic world). Meteorol. Z. 215–226. https://doi.org/10.1127/0941-2948/2011/105

Koven, C.D., Ringeval, B., Friedlingstein, P., Ciais, P., Cadule, P., Khvorostyanov, D., Krinner, G., Tarnocai, C., 2011. Permafrost carbon-climate feedbacks accelerate global warming. PNAS 108, 14769–14774. https://doi.org/10.1073/pnas.1103910108

Kunitsky, V.V., Syromyatnikov, I., Schirrmeister, L., Skachov, Y.B., Grosse, G., Wetterich, S., Grigoriev, M.N., 2013. Ice-rich Permafrost and thermal denudation in the Batagay area (Yana Upland, East Siberia). Earth Cryosphere (Kriosfera Zemli) 17, 56–58.

Lacelle, D., Bjornson, J., Lauriol, B., 2010. Climatic and geomorphic factors affecting contemporary (1950–2004) activity of retrogressive thaw slumps on the Aklavik Plateau, Richardson Mountains, NWT, Canada. Permafrost and Periglacial Processes 21, 1–15. https://doi.org/10.1002/ppp.666

Lacelle, D., Brooker, A., Fraser, R.H., Kokelj, S.V., 2015. Distribution and growth of thaw slumps in the Richardson Mountains–Peel Plateau region, northwestern Canada. Geomorphology 235, 40–51. https://doi.org/10.1016/j.geomorph.2015.01.024

Lalonde, K., Mucci, A., Ouellet, A., Gélinas, Y., 2012. Preservation of organic matter in sediments promoted by iron. Nature 483, 198–200. https://doi.org/10.1038/nature10855

Lavallee, J.M., Soong, J.L., Cotrufo, M.F., 2020. Conceptualizing soil organic matter into particulate and mineral-associated forms to address global change in the 21st century. Global Change Biology 26, 261–273. https://doi.org/10.1111/gcb.14859

Lawrence, D.M., Koven, C.D., Swenson, S.C., Riley, W.J., Slater, A.G., 2015. Permafrost thaw and resulting soil moisture changes regulate projected high-latitude CO_2 and CH_4 emissions. Environ. Res. Lett. 10, 094011. https://doi.org/10.1088/1748-9326/10/9/094011

Leibman, M., Kizyakov, A., Zhdanova, Y., Sonyushkin, A., Zimin, M., 2021. Coastal Retreat Due to Thermodenudation on the Yugorsky Peninsula, Russia during the Last Decade, Update since 2001–2010. Remote Sensing 13, 4042. https://doi.org/10.3390/rs13204042

Martens, J., Mueller, C.W., Joshi, P., Rosinger, C., Maisch, M., Kappler, A., Bonkowski, M., Schwamborn, G., Schirrmeister, L., Rethemeyer, J., 2023. Stabilization of mineral-associated organic carbon in Pleistocene permafrost. Nat Commun 14, 2120. https://doi.org/10.1038/s41467-023-37766-5

McGill, R., Tukey, J.W., Larsen, W.A., 1978. Variations of Box Plots. The American Statistician 32, 12–16. https://doi.org/10.2307/2683468

McGuire, A.D., Lawrence, D.M., Koven, C., Clein, J.S., Burke, E., Chen, G., Jafarov, E., MacDougall, A.H., Marchenko, S., Nicolsky, D., Peng, S., Rinke, A., Ciais, P., Gouttevin, I., Hayes, D.J., Ji, D., Krinner, G., Moore, J.C., Romanovsky, V., Schädel, C., Schaefer, K., Schuur, E.A.G., Zhuang, Q., 2018. Dependence of the evolution of carbon dynamics in the northern permafrost region on the trajectory of climate change. PNAS 115, 3882–3887. https://doi.org/10.1073/pnas.1719903115

Mehra, O.P., Jackson, M.L., 1958. Iron Oxide Removal from Soils and Clays by a Dithionite-Citrate System Buffered with Sodium Bicarbonate. Clays Clay Miner. 7, 317–327. https://doi.org/10.1346/CCMN.1958.0070122

Monhonval, A., Mauclet, E., Hirst, C., Bemelmans, N., Eekman, E., Schuur, E.A.G., Opfergelt, S., 2023. Mineral organic carbon interactions in dry versus wet tundra soils. Geoderma 436, 116552. https://doi.org/10.1016/j.geoderma.2023.116552

Monhonval, A., Mauclet, E., Pereira, B., Vandeuren, A., Strauss, J., Grosse, G., Schirrmeister, L., Fuchs, M., Kuhry, P., Opfergelt, S., 2021a. Mineral Element Stocks in the Yedoma Domain: A Novel Method

Applied to Ice-Rich Permafrost Regions. Frontiers in Earth Science 9, 773. https://doi.org/10.3389/feart.2021.703304
Monhonval, A., Strauss, J., Mauclet, E., Hirst, C., Bemelmans, N., Grosse, G., Schirrmeister, L., Fuchs, M., Opfergelt, S., 2021b. Iron Redistribution Upon Thermokarst Processes in the Yedoma Domain. Front. Earth Sci. 9. https://doi.org/10.3389/feart.2021.703339
Monhonval, A., Strauss, J., Thomas, M., Hirst, C., Titeux, H., Louis, J., Gilliot, A., du Bois d'Aische, E., Pereira, B., Vandeuren, A., Grosse, G., Schirrmeister, L., Jongejans, L.L., Ulrich, M., Opfergelt, S., 2022. Thermokarst processes increase the supply of stabilizing surfaces and elements (Fe, Mn, Al, and Ca) for mineral–organic carbon interactions. Permafrost and Periglacial Processes 33, 452–469. https://doi.org/10.1002/ppp.2162
Mu, C., Zhang, F., Mu, M., Chen, X., Li, Z., Zhang, T., 2020. Organic carbon stabilized by iron during slump deformation on the Qinghai-Tibetan Plateau. CATENA 187, 104282. https://doi.org/10.1016/j.catena.2019.104282
Mu, C.C., Zhang, T.J., Zhao, Q., Guo, H., Zhong, W., Su, H., Wu, Q.B., 2016. Soil organic carbon stabilization by iron in permafrost regions of the Qinghai-Tibet Plateau. Geophysical Research Letters 43, 10,286-10,294. https://doi.org/10.1002/2016GL070071
Mueller, C.W., Rethemeyer, J., Kao-Kniffin, J., Löppmann, S., Hinkel, K.M., G. Bockheim, J., 2015. Large amounts of labile organic carbon in permafrost soils of northern Alaska. Global Change Biology 21, 2804–2817. https://doi.org/10.1111/gcb.12876
Murton, J., Opel, T., Wetterich, S., Ashastina, K., Savvinov, G., Danilov, P., Boeskorov, V., 2023. Batagay megaslump: A review of the permafrost deposits, Quaternary environmental history, and recent development. Permafrost and Periglacial Processes 34, 399–416. https://doi.org/10.1002/ppp.2194
Murton, J.B., Ballantyne, C.K., 2017. Chapter 5 Periglacial and permafrost ground models for Great Britain. Geol. Soc. London Eng. Geol. Spec. Publ. 28, 501–597. https://doi.org/10.1144/EGSP28.5
Murton, J.B., Goslar, T., Edwards, M.E., Bateman, M.D., Danilov, P.P., Savvinov, G.N., Gubin, S.V., Ghaleb, B., Haile, J., Kanevskiy, M., Lozhkin, A.V., Lupachev, A.V., Murton, D.K., Shur, Y., Tikhonov, A., Vasil'chuk, A.C., Vasil'chuk, Y.K., Wolfe, S.A., 2015. Palaeoenvironmental Interpretation of Yedoma Silt (Ice Complex) Deposition as Cold-Climate Loess, Duvanny Yar, Northeast Siberia. Permafrost and Periglacial Processes 26, 208–288. https://doi.org/10.1002/ppp.1843
Murton, J.B., Opel, T., Toms, P., Blinov, A., Fuchs, M., Wood, J., Gärtner, A., Merchel, S., Rugel, G., Savvinov, G., Wetterich, S., 2022. A multimethod dating study of ancient permafrost, Batagay megaslump, east Siberia. Quaternary Research 105, 1–22. https://doi.org/10.1017/qua.2021.27
Natali, S.M., Holdren, J.P., Rogers, B.M., Treharne, R., Duffy, P.B., Pomerance, R., MacDonald, E., 2021. Permafrost carbon feedbacks threaten global climate goals. Proc. Natl. Acad. Sci. 118, e2100163118. https://doi.org/10.1073/pnas.2100163118
Obu, J., Westermann, S., Kääb, A., Bartsch, A., 2018. Ground Temperature Map, 2000-2016, Northern Hemisphere Permafrost. Alfred Wegener Institute, Helmholtz Centre for Polar and Marine Research, Bremerhaven.
Opel, T., Murton, J.B., Wetterich, S., Meyer, H., Ashastina, K., Günther, F., Grotheer, H., Mollenhauer, G., Danilov, P.P., Boeskorov, V., Savvinov, G.N., Schirrmeister, L., 2019. Past climate and continentality inferred from ice wedges at Batagay megaslump in the Northern Hemisphere's most continental region, Yana Highlands, interior Yakutia. Climate of the Past 15, 1443–1461. https://doi.org/10.5194/cp-15-1443-2019
Opfergelt, S., 2020. The next generation of climate model should account for the evolution of mineral-organic interactions with permafrost thaw. Environ. Res. Lett. 15, 091003. https://doi.org/10.1088/1748-9326/ab9a6d
Parfitt, R.L., Childs, C.W., 1988. Estimation of forms of Fe and Al - a review, and analysis of contrasting soils by dissolution and Mossbauer methods. Soil Res. 26, 121–144. https://doi.org/10.1071/sr9880121

Patzner, M.S., Logan, M., McKenna, A.M., Young, R.B., Zhou, Z., Joss, H., Mueller, C.W., Hoeschen, C., Scholten, T., Straub, D., Kleindienst, S., Borch, T., Kappler, A., Bryce, C., 2022. Microbial iron cycling during palsa hillslope collapse promotes greenhouse gas emissions before complete permafrost thaw. Commun Earth Environ 3, 1–14. https://doi.org/10.1038/s43247-022-00407-8

Patzner, M.S., Mueller, C.W., Malusova, M., Baur, M., Nikeleit, V., Scholten, T., Hoeschen, C., Byrne, J.M., Borch, T., Kappler, A., Bryce, C., 2020. Iron mineral dissolution releases iron and associated organic carbon during permafrost thaw. Nat Commun 11, 6329. https://doi.org/10.1038/s41467-020-20102-6

Pisias, N.G., Martinson, D.G., Moore, T.C., Shackleton, N.J., Prell, W., Hays, J., Boden, G., 1984. High resolution stratigraphic correlation of benthic oxygen isotopic records spanning the last 300,000 years. Marine Geology 56, 119–136. https://doi.org/10.1016/0025-3227(84)90009-4

Plaza, C., Pegoraro, E., Bracho, R., Celis, G., Crummer, K.G., Hutchings, J.A., Hicks Pries, C.E., Mauritz, M., Natali, S.M., Salmon, V.G., Schädel, C., Webb, E.E., Schuur, E.A.G., 2019. Direct observation of permafrost degradation and rapid soil carbon loss in tundra. Nat. Geosci. 12, 627–631. https://doi.org/10.1038/s41561-019-0387-6

Poulton, S.W., Canfield, D.E., 2005. Development of a sequential extraction procedure for iron: implications for iron partitioning in continentally derived particulates. Chemical Geology 214, 209–221. https://doi.org/10.1016/j.chemgeo.2004.09.003

R Core Team, ., 2019. R: A Language and Environment for Statistical Computing. Vienna, Austria.

Rantanen, M., Karpechko, A.Y., Lipponen, A., Nordling, K., Hyvärinen, O., Ruosteenoja, K., Vihma, T., Laaksonen, A., 2022. The Arctic has warmed nearly four times faster than the globe since 1979. Commun Earth Environ 3, 1–10. https://doi.org/10.1038/s43247-022-00498-3

Ravansari, R., Wilson, S.C., Tighe, M., 2020. Portable X-ray fluorescence for environmental assessment of soils: Not just a point and shoot method. Environment International 134, 105250. https://doi.org/10.1016/j.envint.2019.105250

Rennert, T., 2019. Wet-chemical extractions to characterise pedogenic Al and Fe species – a critical review. Soil Res. 57, 1–16. https://doi.org/10.1071/SR18299

Salvadó, J.A., Tesi, T., Andersson, A., Ingri, J., Dudarev, O.V., Semiletov, I.P., Gustafsson, Ö., 2015. Organic carbon remobilized from thawing permafrost is resequestered by reactive iron on the Eurasian Arctic Shelf. Geophysical Research Letters 42, 8122–8130. https://doi.org/10.1002/2015GL066058

Savvinov, G.N., Danilov, P.P., Petrov, A.A., Makarov, V.S., Boeskorov, V.S., Grigoriev, S.E., 2018. Environmental problems of the Verkhoyansky Region. Vestnik of North-Eastern Federal University, Earth Sciences 6, 18–33. https://doi.org/DOI: 10.25587/SVFU.2018.68.21798

Schädel, C., Bader, M.K.-F., Schuur, E.A.G., Biasi, C., Bracho, R., Čapek, P., De Baets, S., Diáková, K., Ernakovich, J., Estop-Aragones, C., Graham, D.E., Hartley, I.P., Iversen, C.M., Kane, E., Knoblauch, C., Lupascu, M., Martikainen, P.J., Natali, S.M., Norby, R.J., O'Donnell, J.A., Chowdhury, T.R., Šantrůčková, H., Shaver, G., Sloan, V.L., Treat, C.C., Turetsky, M.R., Waldrop, M.P., Wickland, K.P., 2016. Potential carbon emissions dominated by carbon dioxide from thawed permafrost soils. Nature Clim Change 6, 950–953. https://doi.org/10.1038/nclimate3054

Schirrmeister, L., Dietze, E., Matthes, H., Grosse, G., Strauss, J., Laboor, S., Ulrich, M., Kienast, F., Wetterich, S., 2020. The genesis of Yedoma Ice Complex permafrost – grain-size endmember modeling analysis from Siberia and Alaska. E&G Quaternary Science Journal 69, 33–53. https://doi.org/10.5194/egqsj-69-33-2020

Schirrmeister, L., Froese, D., Tumskoy, V., Grosse, G., Wetterich, S., 2013. Yedoma: Late Pleistocene Ice-Rich Syngenetic Permafrost of Beringia. Encyclopedia of Quaternary Science (Second Edition) 542–552. https://doi.org/10.1016/B978-0-444-53643-3.00106-0

Schirrmeister, L., Kunitsky, V., Grosse, G., Wetterich, S., Meyer, H., Schwamborn, G., Babiy, O., Derevyagin, A., Siegert, C., 2011. Sedimentary characteristics and origin of the Late Pleistocene Ice Complex on north-east Siberian Arctic coastal lowlands and islands – A review. Quaternary

International, Timing and Vegetation History of Past Interglacials in Northern Eurasia 241, 3–25. https://doi.org/10.1016/j.quaint.2010.04.004

Schmidt, M.W.I., Torn, M.S., Abiven, S., Dittmar, T., Guggenberger, G., Janssens, I.A., Kleber, M., Kögel-Knabner, I., Lehmann, J., Manning, D.A.C., Nannipieri, P., Rasse, D.P., Weiner, S., Trumbore, S.E., 2011. Persistence of soil organic matter as an ecosystem property. Nature 478, 49–56. https://doi.org/10.1038/nature10386

Schuur, E. a. G., McGuire, A.D., Schädel, C., Grosse, G., Harden, J.W., Hayes, D.J., Hugelius, G., Koven, C.D., Kuhry, P., Lawrence, D.M., Natali, S.M., Olefeldt, D., Romanovsky, V.E., Schaefer, K., Turetsky, M.R., Treat, C.C., Vonk, J.E., 2015. Climate change and the permafrost carbon feedback. Nature 520, 171–179. https://doi.org/10.1038/nature14338

Shakil, S., Tank, S.E., Kokelj, S.V., Vonk, J.E., Zolkos, S., 2020. Particulate dominance of organic carbon mobilization from thaw slumps on the Peel Plateau, NT: Quantification and implications for stream systems and permafrost carbon release. Environ. Res. Lett. 15, 114019. https://doi.org/10.1088/1748-9326/abac36

Shakil, S., Tank, S.E., Vonk, J.E., Zolkos, S., 2022. Low biodegradability of particulate organic carbon mobilized from thaw slumps on the Peel Plateau, NT, and possible chemosynthesis and sorption effects. Biogeosciences 19, 1871–1890. https://doi.org/10.5194/bg-19-1871-2022

Strauss, J., Abbott, B.W., Hugelius, G., Schuur, E.A.G., Treat, C., Fuchs, M., Schädel, C., Ulrich, M., Turetsky, M., Keuschnig, M., Biasi, C., Yang, Y., Grosse, G., 2021a. Permafrost, in: Recarbonizing Global Soils – A Technical Manual of Recommended Management Practices. FAO, Rome, Italy. https://doi.org/10.4060/cb6378en

Strauss, J., Laboor, S., Schirrmeister, L., Fedorov, A.N., Fortier, D., Froese, D., Fuchs, M., Günther, F., Grigoriev, M., Harden, J., Hugelius, G., Jongejans, L.L., Kanevskiy, M., Kholodov, A., Kunitsky, V., Kraev, G., Lozhkin, A., Rivkina, E., Shur, Y., Siegert, C., Spektor, V., Streletskaya, I., Ulrich, M., Vartanyan, S., Veremeeva, A., Anthony, K.W., Wetterich, S., Zimov, N., Grosse, G., 2021b. Circum-Arctic Map of the Yedoma Permafrost Domain. Frontiers in Earth Science 9.

Strauss, J., Schirrmeister, L., Grosse, G., Fortier, D., Hugelius, G., Knoblauch, C., Romanovsky, V., Schädel, C., Schneider von Deimling, T., Schuur, E.A.G., Shmelev, D., Ulrich, M., Veremeeva, A., 2017. Deep Yedoma permafrost: A synthesis of depositional characteristics and carbon vulnerability. Earth-Science Reviews 172, 75–86. https://doi.org/10.1016/j.earscirev.2017.07.007

Strauss, J., Schirrmeister, L., Grosse, G., Wetterich, S., Ulrich, M., Herzschuh, U., Hubberten, H.-W., 2013. The deep permafrost carbon pool of the Yedoma region in Siberia and Alaska. Geophysical Research Letters 40, 6165–6170. https://doi.org/10.1002/2013GL058088

Tanski, G., Lantuit, H., Ruttor, S., Knoblauch, C., Radosavljevic, B., Strauss, J., Wolter, J., Irrgang, A.M., Ramage, J., Fritz, M., 2017. Transformation of terrestrial organic matter along thermokarst-affected permafrost coasts in the Arctic. Sci. Total Environ. 581–582, 434–447. https://doi.org/10.1016/j.scitotenv.2016.12.152

Thomas, M., Monhonval, A., Hirst, C., Bröder, L., Zolkos, S., Vonk, J.E., Tank, S.E., Keskitalo, K.H., Shakil, S., Kokelj, S.V., van der Sluijs, J., Opfergelt, S., 2023. Evidence for preservation of organic carbon interacting with iron in material displaced from retrogressive thaw slumps: Case study in Peel Plateau, western Canadian Arctic. Geoderma 433, 116443. https://doi.org/10.1016/j.geoderma.2023.116443

Turetsky, M.R., Abbott, B.W., Jones, M.C., Anthony, K.W., Olefeldt, D., Schuur, E.A.G., Grosse, G., Kuhry, P., Hugelius, G., Koven, C., Lawrence, D.M., Gibson, C., Sannel, A.B.K., McGuire, A.D., 2020. Carbon release through abrupt permafrost thaw. Nature Geoscience 13, 138–143. https://doi.org/10.1038/s41561-019-0526-0

Turetsky, M.R., Abbott, B.W., Jones, M.C., Anthony, K.W., Olefeldt, D., Schuur, E.A.G., Koven, C., McGuire, A.D., Grosse, G., Kuhry, P., Hugelius, G., Lawrence, D.M., Gibson, C., Sannel, A.B.K., 2019. Permafrost collapse is accelerating carbon release. Nature 569, 32–34. https://doi.org/10.1038/d41586-019-01313-4

Vadakkedath, V., Zawadzki, J., Przeździecki, K., 2020. Multisensory satellite observations of the expansion of the Batagaika crater and succession of vegetation in its interior from 1991 to 2018. Environ Earth Sci 79, 150. https://doi.org/10.1007/s12665-020-8895-7

van der Sluijs, J., Kokelj, S.V., Fraser, R.H., Tunnicliffe, J., Lacelle, D., 2018. Permafrost Terrain Dynamics and Infrastructure Impacts Revealed by UAV Photogrammetry and Thermal Imaging. Remote Sensing 10, 1734. https://doi.org/10.3390/rs10111734

van der Sluijs, J., Kokelj, S.V., Tunnicliffe, J.F., 2023. Allometric scaling of retrogressive thaw slumps. The Cryosphere 17, 4511–4533. https://doi.org/10.5194/tc-17-4511-2023

von Lützow, M., Kögel-Knabner, I., Ekschmitt, K., Matzner, E., Guggenberger, G., Marschner, B., Flessa, H., 2006. Stabilization of organic matter in temperate soils: mechanisms and their relevance under different soil conditions – a review. European Journal of Soil Science 57, 426–445. https://doi.org/10.1111/j.1365-2389.2006.00809.x

Vonk, J.E., Mann, P.J., Davydov, S., Davydova, A., Spencer, R.G.M., Schade, J., Sobczak, W.V., Zimov, N., Zimov, S., Bulygina, E., Eglinton, T.I., Holmes, R.M., 2013a. High biolability of ancient permafrost carbon upon thaw. Geophys. Res. Lett. 40, 2689–2693. https://doi.org/10.1002/grl.50348

Vonk, J.E., Mann, P.J., Dowdy, K.L., Davydova, A., Davydov, S.P., Zimov, N., Spencer, R.G.M., Bulygina, E.B., Eglinton, T.I., Holmes, R.M., 2013b. Dissolved organic carbon loss from Yedoma permafrost amplified by ice wedge thaw. Environ. Res. Lett. 8, 035023. https://doi.org/10.1088/1748-9326/8/3/035023

Vonk, J.E., Sánchez-García, L., van Dongen, B.E., Alling, V., Kosmach, D., Charkin, A., Semiletov, I.P., Dudarev, O.V., Shakhova, N., Roos, P., Eglinton, T.I., Andersson, A., Gustafsson, Ö., 2012. Activation of old carbon by erosion of coastal and subsea permafrost in Arctic Siberia. Nature 489, 137–140. https://doi.org/10.1038/nature11392

Vonk, J.E., Tank, S.E., Walvoord, M.A., 2019. Integrating hydrology and biogeochemistry across frozen landscapes. Nature Communications 10, 5377. https://doi.org/10.1038/s41467-019-13361-5

Wagai, R., Mayer, L.M., 2007. Sorptive stabilization of organic matter in soils by hydrous iron oxides. Geochimica et Cosmochimica Acta 71, 25–35. https://doi.org/10.1016/j.gca.2006.08.047